A BULK COMPUTATIONAL HEAT TRANSFER MODEL FOR USE AS A PREDICTIVE DESIGN TOOL

A Thesis

Submitted to the Office of Graduate Studies
of Saint Martin's University
in Partial Fulfillment of the Requirements
for the Degree of

Master of Mechanical Engineering

by

Shelby Ann Ferguson, B.S.M.E.

Paul E. Slaboch, Director

Graduate Program in Mechanical Engineering
Lacey, Washington
August 28, 2015

A BULK COMPUTATIONAL HEAT TRANSFER MODEL FOR USE AS A PREDICTIVE DESIGN TOOL

Abstract

by

Shelby Ann Ferguson

The development of a bulk computational heat transfer model to simulate a four zone heater design of an internal heat generating device was investigated. Theoretical conduction heat transfer equations were solved to create orthotropic materials which simulated the composite material construction and discrete structures of the real device. Theoretical average convection surface heat transfer coefficients were calculated and applied as the primary boundary conditions in the simulation. Heater zone shape simplifications were applied to simplify the complex internal heater geometry of the device in order to produce a rectangular computational model for quick-turn thermal analyses.

A variety of single and multiple zone experimental studies were completed for comparison to corresponding single and multiple zone computational studies. The power and thermal data from experimental studies were compared to computational results. The resulting singular zone computational contour plots agree well with the corresponding experimental contour plots. Offsets between the absolute temperatures of the experimental and computational studies were observed. Suggestions for improving the bulk computational model were presented, as well as next steps for furthering the development of the model and its' use as predictive analytical tool.

To my parents, Terri and Gregory Ferguson, for the never ending love and support in everything that I do.

ACKNOWLEDGMENTS

I would like to thank my advisor, Dr. Paul Slaboch, for his help and guidance through this process.

I would also like to thank my mentor, Russell Aoki, for his direction and encouragement.

CONTENTS

FIGURES

TABLES

SYMBOLS

English

A	cross-sectional area
c_p	Material specific heat
g	Gravity
k	Material conductivity
L	Length
L_1	All zone generalized length
$\overline{Nu_L}$	Nusselt number
Pr	Prandtl number
$\overline{Ra_L}$	Rayleigh number
R	Material resistance
T	Temperature
w_1, w_2	Zone 2 generalized depth and width, respectively
w_3, w_4	Zone 1 generalized depth and width, respectively
X, Y, Z	Cartesian coordinate system

Greek

α	Thermal diffusivity
β	Inverse film temperature
ρ	Material density
ν	Kinematic viscosity

Subscripts

∞	Ambient

cu, N	Copper, normal
cu, P	Copper, in-plane
eqv, N	Equivalent, normal
eqv, P	Equivalent, in-plane
f	Film
FR, N	FR-4 material, normal
FR, P	FR-4 material, in-plane
$FR-4$	FR-4 material
max	Maximum
min	Minimum

CHAPTER 1

Introduction

1.1 Reason and Purpose

Temperature is a crucial parameter of performance in the computing industry. The cornerstone of computer efficiency and performance depends on the component and environmental temperature in which the machine operates. Decades of engineering resources have been expended in order to develop effective thermal solutions for components that populate computer motherboards and contribute to the function of the machine. Aluminum, copper, or a combination of aluminum and copper heat sinks are the most widely employed thermal solutions used on motherboards to date. Heat sinks work in conjunction with varying types of retention mechanisms and thermal interface materials to assist in necessary heat transfer between the operating component and it's environment. Each thermal solution is exclusively designed for the type of component it will be cooling. Thermal solution design is highly dependent upon the use condition and the overall computer performance expectation.

In order to fully understand how critical it is to design a proper thermal solution and take precautions to ensure solution functionality, a study was completed to consider the absence of a thermal solution for a high powered component such as a high performance central processing unit (CPU). To understand a situation where the connection between a high powered component and its' thermal solution has been broken and is nonexistent, a heat generating vehicle was developed with the purpose of simulating the extreme temperatures that the high powered component could reach with the goal of studying the impacts to the

component, the surrounding elements, and the motherboard. The vehicle developed for the study is referred to as the acronym ISRD in this paper.

The ISRD serves as a self-heating device which can reach the temperatures of interest as they pertain to this investigation. In order to develop a vehicle that can meet the necessary requirements for this project, standard substrate and motherboard characteristics were repurposed. A simplified CPU substrate design is the resulting device. CPU substrates serve the purpose of breaking out and transmitting signals between the CPU silicon and the motherboard by use of vias. In essence, a package substrate is a miniature motherboard with thousands of small copper connections that link specific points from the silicon onto the motherboard. By manipulating the purpose of a substrate design, the ISRD was developed and met the requirements necessary to complete the study.

This thesis will study the the development of a bulk computational heat transfer model to simulate the real ISRD heater design. The goal of developing a computational ISRD model is to investigate if by making simplifications to the intricate ISRD design for predictive modeling purposes, an estimate of the heater design thermal capability can be predicted. The theory and process behind building the ISRD computational model will be discussed and empirical data that was used for model correlation will be presented and compared to the final computational results.

1.2 Market and Literature Research

This thesis discusses the study of a device which produces internally generated heat with the capability of reaching extreme temperatures for experimental purposes. A general Sn-Ag-Cu (SAC305) solder reflow process envelopes the minimum and maximum peak temperatures that would typically be seen during a thermal solution failure, and therefore it was chosen as a comparative baseline for the thermal investigation of this research. Background research into the solder reflow processes was necessary in order to understand the variables that have driven the development of current reflow profiles to date.

1.2.1 Reflow Profile

To understand the controls that are used to accomplish successful solder reflow, research into standard ball grid array (BGA) solder reflow processes was completed. The Solder Technology Handbook describes general solder reflow process, equipment technology, and equipment selection.[1] For the purpose of this thesis, general solder reflow processes is of most interest. The Solder Technology Handbook discusses the general process variables that need to be controlled in order to produce high quality solder joints. The five main variables that must be controlled are materials, machines, manpower, methods, and the environment.[1] While there are several different types of soldering ovens that are employed, each machine is utilized while adhering to a strict set of reflow profile guidelines. Established and adhered to reflow profile requirements are detailed in the Solder Technology Handbook, as producing high quality, low defect solder joints. Even more specifically the handbook states that it does not matter how the heat is applied to the solder joints as long as the heat is applied in a controlled manner. To control the manner in which heat is applied to solder joints, reflow profiles have been developed.[1]

Reflow profiles are dependent on the type of solder compound material that is being

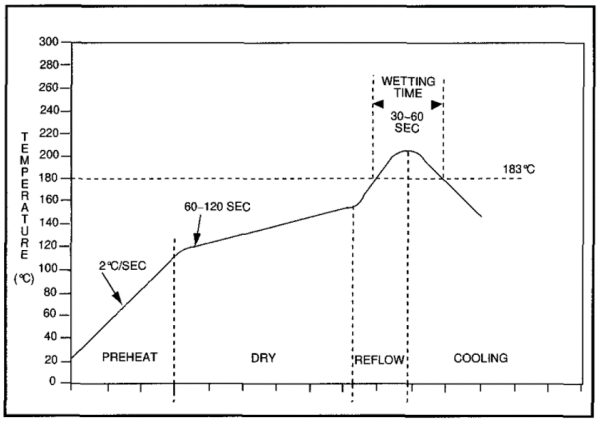

Figure 1.1: Solder Technology Handbook Reflow Profile

worked. Different types of solder composites will require various reflow profiles. Figure 1.1 is taken from page 3 of the Solder Technology Handbook and presents a generic reflow profile, with a definition of the function of each section that comprises the profile. Four sections exist, each with a specific purpose. The first zone, the preheat ramp, is specified in order to minimize thermal shock to the components and the full motherboard assembly. It is also used as a safety guard against solder joint spattering that can occur as the moisture inside the solder joint begins to evaporate and outgas as temperature rises dramatically. A ramp rate of no more than $2°C/s$ is specified for this section.[1] The second ramp zone, referred to as dry out in the figure but has also been called soak, or preflow, is used to ensure that the solder paste has fully dried before entering reflow temperature ranges.[1] The third zone, is the reflow zone, and is responsible for the temperature ramp between the minimum and maximum reflow temperatures. As a guideline, the handbook states, that solder should be elevated by approximately 20°C over its minimum reflow temperature specification in order to ensure quality reflow.[1] The wetting time zone is the time above reflow. This is the amount of time that the solder is held in the liquidous state. Intermetallic compound (IMC) layers within solder joints form as a function of time above reflow temperatures. IMC layers are a contributing factor to poor solder joints, as they are a brittle composite material that is formed between the elements found in the solder joints and the surface elements to which the solder material is being attached. These compound materials can create points of brittleness within the solder which can eventually lead to fatigue failures of the solder joints over time. Therefore, time above reflow is a critical parameter that must be controlled in order to produce quality solder joints.[1]

While there is a typical profile that should be adhered to in order to ensure assembly and solder joint quality after the reflow process has completed, like any other process, natural variation will occur. Page 5 of the Solder Technology Handbook presents Figure 1.2 to demonstrate the solder reflow process upper and lower boundary limits that may be acceptable depending on the temperature limits of the specific solder material being evaluated.

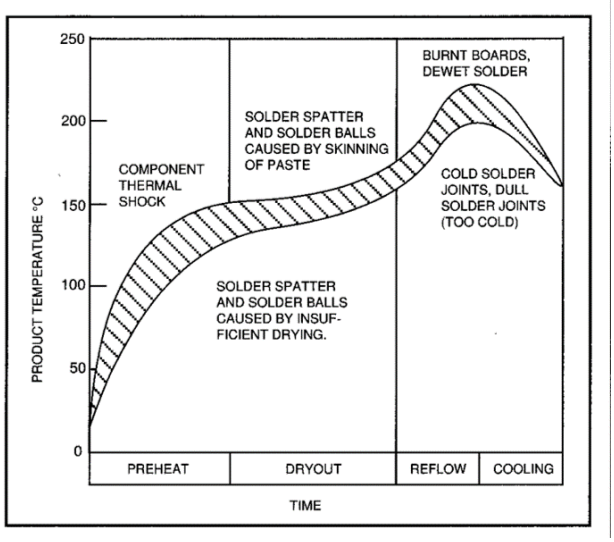

Figure 1.2: Solder Technology Handbook Reflow Profile Band

The purpose of the ISRD for this study is to reach extreme temperatures that could possibly be seen during a thermal solution failure. However, since the ISRD is designed with the capability of following a solder reflow profile, the ISRD could be repurposed to act as a primary soldering device. Research into vehicles that have the primary purpose of reflowing solder was completed. While there is minimal material available as to existence of such devices used for the purpose of localized solder reflow, research for this thesis discovered a patent established for an invention that uses the power of inductive heating to create quality solder joints. The invention is discussed in the following paragraphs of this section.

A United States Patent, number US 6,229,124 B1 has been granted to the invention of an in situ soldering process through use of localized electromagnetic induction heating. The inventor and patent owner, Horacio Andres Trucco of Melville, New York, describes his Inductive Self-Soldering Printed Circuit Board invention as an alternative method of creating solder joints, to the traditional oven reflow and wave soldering processes.

The inductive self-heating printed circuit board utilizes a solenoid supplied with an alternating current which generates a variable magnetic field and induces eddy currents inside an

adjacent metal bar. The eddy currents are then converted to heat by the Joule effect.[2] The method of electromagnetic induction heating (EIH) only allows energy to be transferred to conductive bodies. Therefore, the use of (EIH) avoids heating up any part of the component that is an insulating material. Heat is only applied to the solder, leads, and corresponding pads in a PCB.[2]

The electromagnetic induction heating process is said to be faster and will utilize approximately 200 times less energy than the traditional conductive/convective reflow processes.[2] By keeping heat localized to only the conductive materials in the region where soldering is desired, the surrounding PCB and other components are not subjected to extreme temperatures. This greatly decreases and nearly eliminates the risk of damaging components and solder connections due to thermal failure mechanisms such as: thermal shock, pop-corning effect, and the development of intermetallic compound layers.[2]

The objective of the described invention is to act as an in situ soldering process that is capable of soldering surface mount components to the motherboard without heating up the areas which are unnecessarily heated in standard industry reflow processes. Although the purpose of the Inductive Self-Heating Printed Circuit Board invention and the ISRD serve different purposes, as mentioned previously, the ISRD could be repurposed to act as a localized soldering device. However, it would not have produce the same benefits as the invention described, since the ISRD uses resistive trace heating and thereby allows heat to spread to metallic and nonmetallic materials, unlike the EIH process.

1.2.2 Thermal Computational Analyses

This thesis focuses on the development of a bulk computational model to simulate the thermal capabilities of the ISRD heater design. Research was completed on similar studies that have investigated bulk model creation and comparison to corresponding detailed models. Various methods of bulk model creation and use are discussed in this section. Research in this section focuses on work pertaining to bulk model creation for simulation of computing

technology.

Ma, et al. developed an effective model for thermal conduction analysis for $2.5D$ packaging through use of a through silicon via (TSV) interposer.[3] The study compared the results of a simplified computational model that utilized the calculated effective thermal conductivities versus the detailed real model which included via geometry and normal material property assignment. The effective thermal conductivities in this study were developed by considering a simple parallel model to predict the out-of-plane effective thermal conduction. The in-plane effective thermal conductivity was derived on the basis of heat balances. Results from the equivalent computational model proved to be within 95% of the detailed real model.[3]

Xing et al., completed a numerical simulation of micro-bumped flip chips mounted on TSV interposers to study the thermal performance of a package. [4] A volume averaging method was employed to determine the effective thermal conductivity for in-plane and out-of-plane directions to accomplish a simplified thermal model and characterization of the package with a through-silicon-vias (TSVs) interposer.[4] All simulations in this study were computed in Ansys Icepak and the simplified model showed reasonably good results.[4]

To estimate the equivalent thermal conductivity of TSVs in 3D IC integration, Chien et al. studied multiple variables that affected the thermal conductivity in the longitudinal, transverse, and perpendicular directions of the package.[5] Through utilization of Ansys Icepak, they extracted equivalent thermal conductivities of the different variables tested in a semi-3D heat transfer conduction model for comparison to a detailed model which embodied the real TSVs structures. The results proved to be in good agreement with the simulation errors for K_{xy} and K_z, falling within $10 - 15\%$.[5]

As part of the paper written by Hoe, et al., the effects of TSV parameters on the equivalent thermal conductivity of a TSV interposer were considered.[6] The study proved that with decreased via pitch and increased TSV plating in partially filled TSVs, and using a highly conductive filler material would greatly increase the equivalent thermal conductivity of the

TSV interposer.[6]

A paper written by Culham and Yovanovich studied the factors affecting the calculation of effective conductivity in printed circuit boards. The study considered three different design options that have varying influence on the calculation of an effective conductivity to be used to represent the true thermophysical behavior of a multilayer board.[7] The variables considered were: relative location of high and low conductivity layers in relation to a heat source boundary, heat source size and location, and convective boundary conditions.[7] Culham and Yovanovich found that when considering the previously mentioned variables, it was essential to consider the role of spreading resistance when calculating the effective conductivity for a typical electronic printed circuit board (PCB). Since series and parallel resistance paths are commonly used to calculate effective conductivity, the influence of internal layer location to the PCB, package density, and heat source placement are often omitted and are a major source of error.[7] The magnitude of each variables influence on the calculated effective conductivity was further discussed in the conclusion of the paper.

In the preceding sections an introduction to the work of this thesis has been presented. Research pertaining to solder reflow, an in situ reflow device, and similar computational heat transfer models has been discussed. The following chapters will present a detailed discussion of the work completed for this master's thesis. The overall ISRD design will be explained in order to clearly identify the attributes that were significant for the development of the computational ISRD model. Equivalent material properties will be derived based on theoretical heat transfer conduction equations and volumetric averaging methods in order to simulate the varying zone properties throughout the ISRD body. Experimental and computational results will be compared in order to determine if the theoretical equivalent material properties and boundary conditions applied in the computational simulation resulted in an analytical tool that could be used for future ISRD heater design thermal analysis.

1.3 Introduction to the ISRD Design

The real ISRD is assembled of standard CPU substrate materials; copper and FR-4. Resistive copper heating traces, $0.0762mm$ in width, are etched into the first internal layer of the ISRD, $0.2032mm$ below the top surface. A schematic of the ISRD cross section is shown in Figure 1.3 (schematic not drawn to scale). The ISRD contains 1,667 vertical

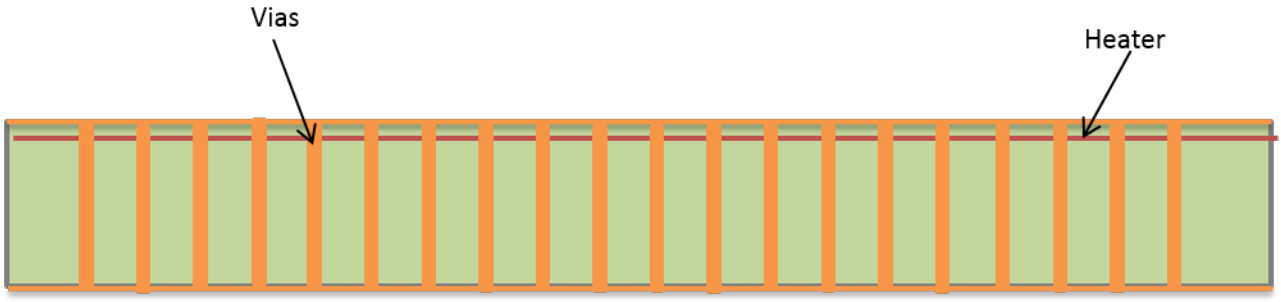

Figure 1.3: Cross sectional ISRD Schematic

columns that travel through the vehicle body from top to bottom surface. The columns are referred to as vias. Vias are traditionally utilized as a connection path in which signals on a motherboard travel from layer to another. They are also used in package substrates to connect a pin from the silicon through the package to the motherboard surface. For this study, the vias within the ISRD are repurposed to carry energy from internally generated heat to the external surfaces of the ISRD. One can accurately visualize a via as a small copper wire typically on the scale of $0.013mm$ in diameter when used in package substrates or motherboards. There are two types of vias: filled vias and plated through hole vias. A filled via simply describes the vias as a solid column of material, and a through hole via implies the opposite; the via is a hollow cylinder and thereby a wall thickness is associated with the column. Vias within the ISRD are plated through hole vias constructed of copper with a diameter is $0.13mm$ and a wall thickness of approximately $0.9mm$.

In Figure 1.4, a plan view of the ISRD board file and its' internal heater traces are shown.

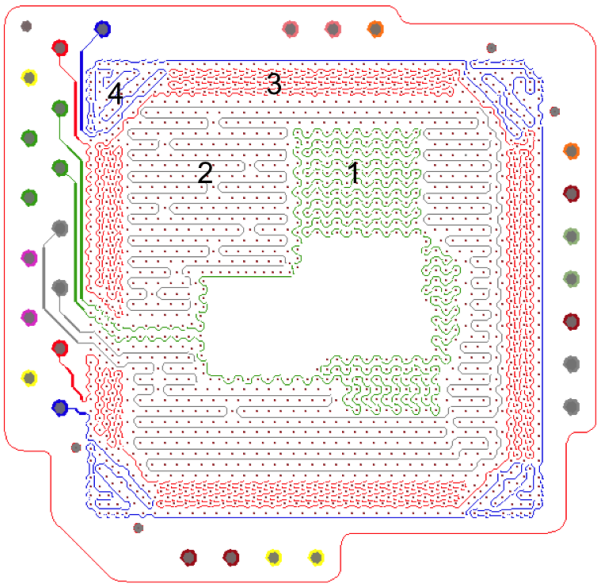

Figure 1.4: Real ISRD Board File Image

The single red exterior line is the outline of the ISRD and the varying colored internal lines are the resistive heaters located on the first layer below the vehicle's top surface. The different colored dots in the exterior portion of the body between the red exterior line and the internal heater traces, are the locations in which power is supplied to the ISRD. Notice that each different colored trace is routed to two corresponding power pads. The green, grey, red, and blue heater traces each have two respective power pads, indicating that each internal trace is independent and can be controlled individually. Different ampere values can be applied to each trace resulting in varying power and heat within each zone.

Four separate heater traces can be observed in Figure 1.4. The heater traces identify the four zones which divide the ISRD. The four zones and the respective heater traces are based on varying via pitch observed across the surface of the real ISRD. Via pitch is defined as the spacing between the center of one via to the center of the adjacent via. In Table 1.1, the via pitch values are tabulated by zones as labeled in Figure 1.4. Via pitch and via density are related. A large via pitch will result in a lower via density per unit area, while a small via

TABLE 1.1

Zone Via Density

Zone	Pitch (mm)
1	0.5
2	0.8
3	0.4
4	0.75

pitch will result in a higher via density. Pitch and density will be used interchangeably to describe the via population in each region.

The knowledge of the real ISRD properties discussed here are used in the subsequent chapters of this paper to create geometrically accurate local and bulk models to analytically study the ISRD thermal capabilities.

CHAPTER 2

Computational Analysis

2.1 Ansys IcePak 15.0

All simulations discussed in this thesis were completed in Ansys IcePak v15.0. IcePak is a powerful software package that provides thermal computational capability for a wide range of applications. For this study IcePak was used exclusively as a steady state conduction computational tool to solve the detailed and bulk models described in later sections. IcePak utilizes the Fluent solver, which is the standard solver for Ansys products. An established library with an extensive list of material properties is available for import to simulations within IcePak.

2.2 Detailed Local Model

A detailed local model was created to study the internal ISRD structures and their response to internally generated heat. This detailed computational model is termed "local" as it is a three unit cell model of a particular zone within the ISRD and is comprised of the actual discrete structures which comprise the real ISRD. The detailed local model presented in this section differs from the bulk model in terms of purpose and model structure. The global model will be discussed later in this chapter.

The local model is used as a geometrically accurate simulation to confirm the hypothesized isotherm vector direction within the ISRD. The hypothesis of the local model study predicts that the heat will conduct from the heat sources, laterally through the surrounding

FR-4 material until it reaches the nearest copper via, at which point the direction of energy travel will change and follow the path of least resistance. In this case, the path of least resistance is the copper vias, based on the high conductivity property inherent to copper material. The results from the local model studies are the basis for material properties and boundary conditions assignment in the global model.

Figure 2.1 shows a transparent isometric view of the local model. It is comprised of three

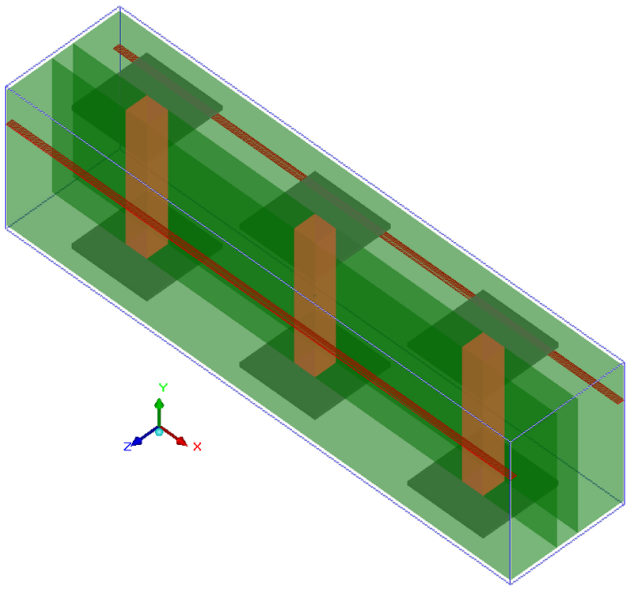

Figure 2.1: Isometric View of ISRD Detailed Local Three Unit Cell Model

unit cells from a particular zone within the ISRD. The green material is made of individual rectangular prisms which represent the solid ISRD body. The green blocks are assigned standard FR-4 material properties, as defined within the Ansys IcePak material library, with conductivity being of most interest to this study at $k = 0.35 W/m^2K$. The orange columns running through the thickness of the FR-4 material are the vias. From the IcePak standard material library, pure copper material properties are assigned to the rectangular vias. IcePak specifies the pure copper as having a conductivity of $387 W/m^2K$, density of $8933 kg/m^3$, and a specific heat of $381 J/kgK$. Both the pure copper and the FR-4 are applied as isotropic materials in the local model. The FR-4 and copper via entities are specified as solid conducting

rectangular blocks. Each of the FR-4 blocks' internal surfaces are mated to the surrounding structures, eliminating air gaps. Because all surfaces are specified as conducting solids with mated surfaces, IcePak assumes the conducting blocks act as an singular continuous structure and thereby ignores the contact surface of the internal mating surfaces.

The double red lines traversing through the FR-4 material on either sides of the vias are the resistive copper heater traces which occupy the three unit cell area. The heater traces are modeled as zero thickness heat sources. A constant power input (W) is specified for the sources. The transparent blocks, situated on the top and bottom of the FR-4 material centered atop each via, are the copper pads. The pads have the same applied material properties as the vias.

Each via is spaced $0.89mm$ apart from one another (edge to edge). The thickness of the FR-4 block structure is $0.8128mm$ and the vias extend from Y_{max} to the Y_{min} surface, through the entirety of the ISRD. The heat sources are situated $0.2032mm$ below the Y_{max} surface. Each of the two heat sources is $0.0381mm$ in width to represent half the width of the actual ISRD heater traces. Although the real heater traces are $0.0762mm$ in width, this model is constructed of unit cells, and only half the width of a heater trace will pass through a via's unit cell area.

A cabinet enclosure surrounds the three unit cell model. The cabinet volume is the only area in which IcePak will apply a mesh and compute a solution. For the three unit cell model pictured in Figure 2.1, the FR-4 blocks, vias, and copper pads are entirely enclosed within the cabinet walls and the outer surfaces of the outer most objects are in contact with the cabinet walls. Therefore, the boundary conditions applied to the cabinet walls will determine the interaction between structures within the cabinet and the surrounding ambient air. Ambient air is set at 20°C, radiation is turned off and the natural convection gravity vector is turned on in this model. The natural convection function will determine the buoyancy driven flows acting on the cabinet's external surfaces. An arbitrary heat transfer coefficient of $50W/m^2K$ is applied to the Y_{max} and Y_{min} surfaces of the cabinet

walls. The focus of the thermal analysis of the detailed local model is the contour plots rather than the absolute temperatures, so the heat transfer coefficient was not calculated but rather was arbitrarily chosen. The X_{max}, X_{min}, Z_{max}, and Z_{min} walls of the cabinet are set as adiabatic walls, with periodic boundary conditions applied to each side. Since the three unit cell model comprises a very small portion of the larger via pattern, applying a periodic boundary condition to the surrounding sides simulates a repeating via/heater trace pattern surrounding the three unit cells under consideration. The model is a steady state, conduction-only simulation study.

2.2.1 Sensitivity Studies

Sensitivity studies were completed on the three unit cell model, shown in Figure 2.1, before delving into the global model with the goal of understanding the basic conductive heat transfer that was hypothesized to take place internally to the ISRD. In Figure 2.2 and Figure 2.3, contour plots from the baseline thermal analysis of the three unit cell model are

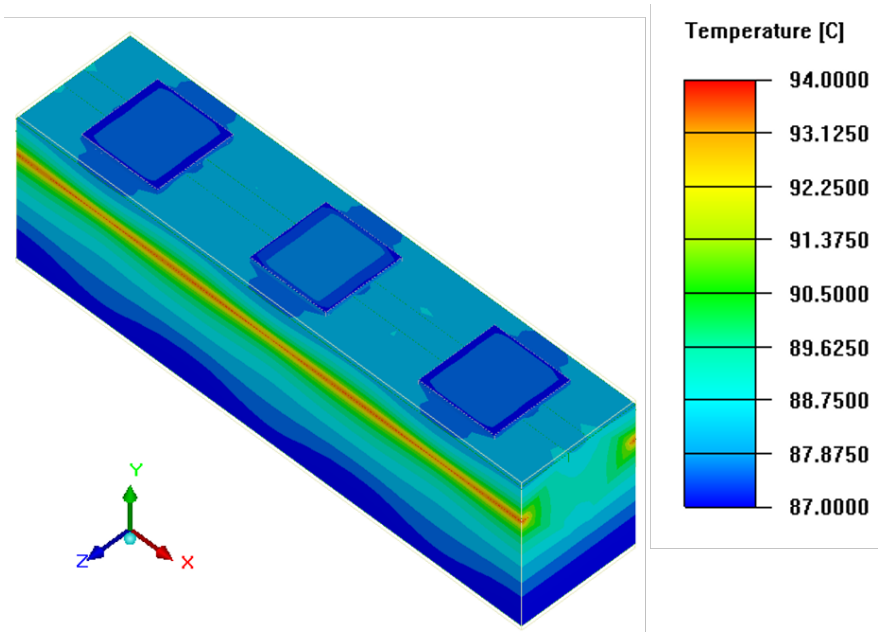

Figure 2.2: Baseline Computational Local Model External Contour Plot

shown in isometric and in-plane cross-section views, respectively. These contour plots serve as a baseline comparison to the concurrent sensitivity studies.

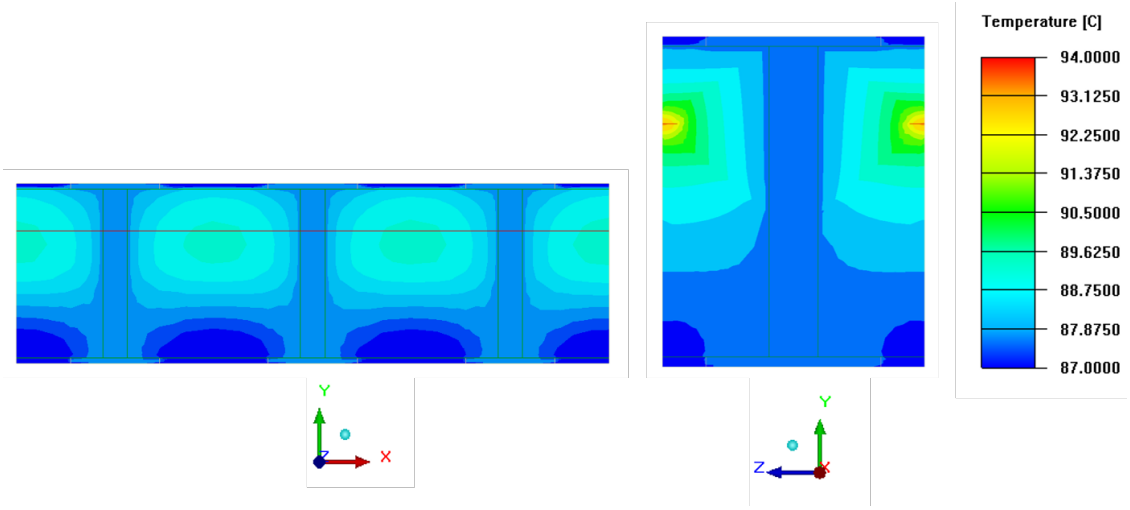

Figure 2.3: Internal Temperature Distribution Between Three Unit Cells

The contour plots from Figure 2.3 show the heat transfer that will take place between the resistive heater traces, the FR-4 material, and the copper vias. The Z_{max} and X_{max} cross-sectional views show a concentration of heat occurring in the FR-4 material between the three vias. In the Z_{max} view, the maximum temperature observed in the interstitial space between the vias is 89.3°C and the temperature in the vias is 87.9°C. Although the difference between the FR-4 and copper material is only 1.4°C, the contour plots are of more interest. The increased heat in the FR-4 regions between the vias can be attributed to the conductive properties of FR-4. FR-4 material is approximately 100 times less conductive than the copper material. Because of its' poor conductive performance, heat takes longer to travel through the material and therefore hot spots will develop in the regions of high resistance materials within the ISRD. The baseline analysis demonstrates that for any unit cell within the real ISRD there will be a temperature difference between the copper via and the adjacent FR-4 material. Through observation of Figure 2.3 the hypothesis pertaining to vector heat flow is confirmed.

After baseline results were understood, the via spacing in the local model was altered. Two of the three vias were moved closer together in order to reduce their pitch. With the altered spacing, distance between two vias was $0.79mm$ and the distanced to the unmoved via was $0.99mm$. By changing the spacing between the vias in the local model, resulting effect of varying pitch on internal hot spots could be observed. The resulting internal contour plots from this sensitivity study can be observed in Figure 2.4.

On the left is a cross-sectional view of the X plane through the FR-4 material between

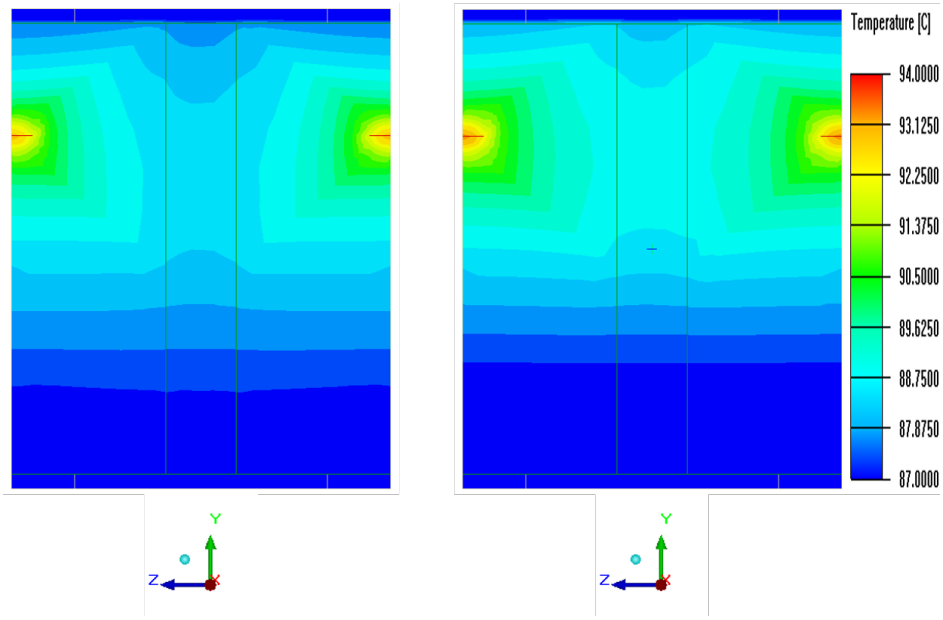

Figure 2.4: Local Contour Plot Comparison: Small vs. Large Pitch

the closely spaced ($0.79mm$) vias and on the right is a cross-sectional view through the FR-4 material between the far spaced via ($0.99m$). The temperature between the close pitched vias and the wide pitched via is 87.5°Cand 88.9°C, respectively. The computational model is predicting that the temperature will rise when the via pitch is increased and it will drop when the via pitch is decreased. These computational results agree well with the hypothesis presented at the beginning of this section. The more tightly the vias are spaced, the more paths of low resistance are available, and therefore the increased conduction heat transfer

from the internal heater traces to the copper vias and finally to the top and bottom surfaces of the ISRD.

2.3 ISRD: Bulk Computational Model

The process for creating the bulk global model is described in this section. Previously, a local model was studied to understand the thermal interaction between discrete structures internal to the ISRD. Results from the local model studies are used to create a model which simulates the ISRD in it's entirety. Material properties, accurate zone geometry and external conditions of the bulk model will be discussed here. Each of these parameters have an impact on the accuracy of the computational model as well as the heating capability and thermal gradients in the real ISRD. The magnitude of each parameters' impact will be compared later in this paper.

2.3.1 ISRD: Model Build Preparation

To prepare for the computational heat transfer analysis it is important to understand the set up and simulation build process. The ISRD has four independent heater zones which need to be realistically portrayed in the IcePak model. Since the end purpose of the bulk computational model is to supply a quick turn thermal analysis on proposed routing schemes, it is desired to produce a model that can deliver an accurate portrayal of the expected thermal gradients and corresponding absolute temperatures in a short time period. To achieve this, it was necessary to make approximations in order to keep the models' geometry simple and rectangular allowing the solver to reach a quick solution with a low mesh count. The simplifications and approximations that were made are discussed in this section.

The global model is described as a "bulk" representation of the real ISRD because the material properties, geometry and boundary conditions are calculated as averages and equivalents of the real ISRD. The process and reasoning for development of the average conditions will be discussed in this chapter. In preparation for model geometry set up, actual heater

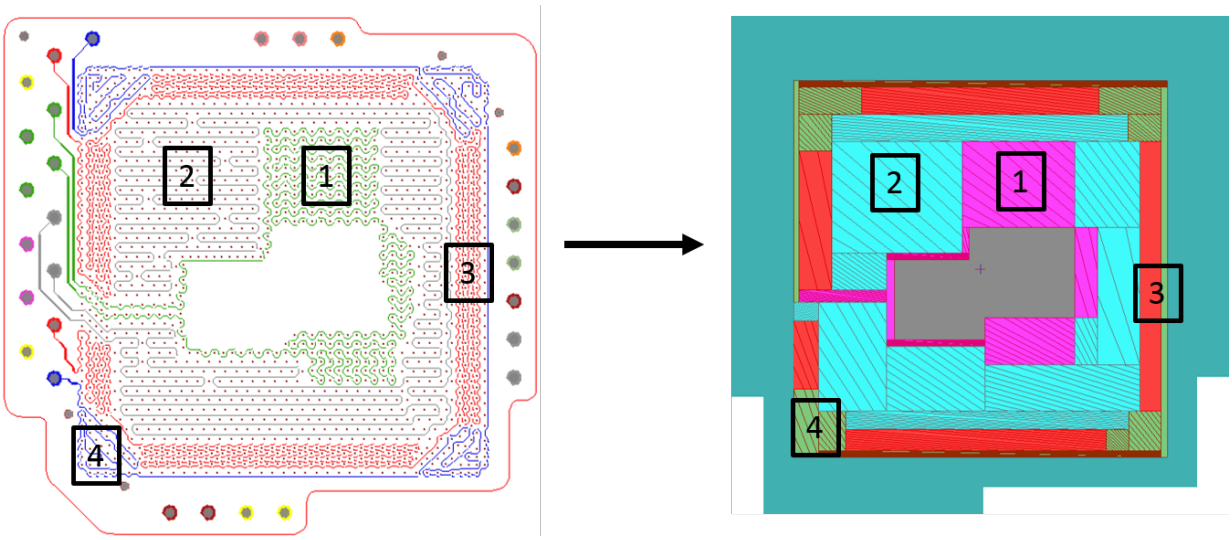

Figure 2.5: Real ISRD versus Modeled ISRD

zone shape in the ISRD was transformed into rectangular geometry that could be easily created in Icepak. In Figure 2.5 shows the top down view of the ISRD heater traces on the left and the resulting zone transformations in the computational model on the right. Each zone was divided into the number of blocks that are needed to accurately copy the actual heater zone shapes. There are a total of 36 blocks that construct the four heater zones and Table 2.1 summarizes the number of blocks that create each independent zone.

TABLE 2.1

Zone Block Numbers

Zone	Number of Blocks
1	8
2	11
3	5
4	12

TABLE 2.2: Zone Block Percents

Zone	**Block Title**	**Percentage, %**
Zone 1	Zone1_1	2.8
	Zone1_2	0.9
	Zone1_3	51
	Zone1_4	11
	Zone1_5	22.3
	Zone1_6	3.4
	Zone1_7	3.1
	Zone1_8	5.5
Zone 2	Zone2_1	23
	Zone2_2	12.3
	Zone2_3	8.8
	Zone2_4	9.1
	Zone2_5	1.7
	Zone2_6	11.6
	Zone2_7	7.9
	Zone2_8	10
	Zone2_9	11.7
	Zone2_10	3.2
	Zone2_11	0.73
Zone 3	Zone3_1	18.4
	Zone3_2	22.9
	Zone3_3	22.9

Table continues on next page

Continued from previous page

Zone	**Block Title**	**Percentage, %**
	Zone3_4	28.9
	Zone3_5	7
Zone 4	Zone4_1	7.1
	Zone4_2	6.7
	Zone4_3	8.4
	Zone4_4	13.5
	Zone4_5	8.3
	Zone4_6	4.9
	Zone4_7	13.7
	Zone4_8	7.1
	Zone4_9	2.7
	Zone4_10	12.3
	Zone4_11	6
	Zone4_12	9.5

The surface areas between the real and modeled ISRD are presented to show that they are not exactly the same. Surface area size for the modeled ISRD is a parameter that was approximated in order to quickly build model geometry. So while the modeled surface areas are not exactly the same as the actual surface area values, each modeled zone is measured to be within $40mm^2$ of the real zone surface area value. For the purposes of this bulk model, $40mm^2$ surface area accuracy is acceptable.

The total area of the heater zones in the real ISRD equate to $1,186.7mm^2$ while the modeled heater zone total area equates to $1{,}251.9mm^2$. The modeled ISRD has a surface area of approximately $65.2mm^2$ larger than real ISRD heater zone area. However, the percentage of individual heater zone area to total heater zone area of the modeled versus real ISRD are

TABLE 2.3

Real vs. Modeled Surface Area Comparison

Zone	Real Surface Area (mm^2)	Modeled Surface Area (mm^2)	Real (%)	Modeled (%)
1	184.8	189.7	15.6	16
2	594.2	637.9	50.1	50.1
3	226.4	246.1	19.1	19.7
4	180.7	178.2	15.2	14.2

essentially equivalent, as can be observed in Table 2.3. However, this difference in surface area could potentially be a parameter that builds error into the absolute temperature values and should be noted when comparing experimental and computational data in the later chapters.

2.3.2 ISRD: Power Percentage Allocations

Once the modeled ISRD is built to be within an appropriate size of the actual ISRD, the next step is applying the correct amount of power to each block within the four zones. All blocks of zones 1 through 4 must be allocated a certain percentage of the total power that is applied to each zone, based on the percentage of surface area that an individual block inhabits within its' respective zone. For example, block 1 from zone 1 has a measured surface area of $5.32mm^2$ while zone 1 has a total surface area of $189.7mm^2$. Therefore, block 1 inhabits 2.8% of the total area of zone 1, so it will be allocated 2.8% of the total power to be distributed uniformly across the zone 1 surface area. Table 2.3.1 summarizes the percentages that each block inhabits in zones 1 through 4.

2.3.3 Bulk Material Assignment

The real ISRD, is constructed of two different materials with dissimilar material properties. Part of this study defines the equivalent material that most accurately captures the

true conductivity of the ISRD. The equivalent conductivity of the material is defined as orthotropic to implement proper directional heat transfer that will take place internally within the ISRD based on the local model studies from Section 2.2. The process of calculating and assigning equivalent material properties for the 36 blocks that define the bulk global model will be discussed in this section.

The materials assigned to Zones 1 through 4 in this study will be referred to as "bulk" materials, as they were each created based on the ratio of FR-4 and copper in each zone. When the new materials are assigned to the individual blocks in the modeled ISRD, solid blocks will be created that are entirely constructed of the bulk material property. Hence the blocks will not have discrete via structures built inside of them like the real ISRD. The assigned materials will have appropriately balanced conductivity, density, and specific heat values, based on the ratio of FR-4 and copper in each zone.

Since the density and specific heat of the material are independent of direction, the method for determining the equivalent density and specific heat values differs from the method for determining the effective conductivity. The density and specific heat bulk material properties were derived by performing a volumetric averaging calculation of FR-4 and copper density and specific heat properties. The entire ISRD was considered when equating the volumetric average of these material properties. Therefore, the density and specific heat values are based on the total volume of FR-4 and copper within the ISRD. The bulk material properties for density and specific heat assigned to each block in the heater zone area of the modeled ISRD are: $\rho = 1390.4\ kg/m^3$, and $c_p = 1279.9\ J/kg$, respectively.

The conductivity material property assignment for the bulk global model is based exclusively on the differing via pitches within the ISRD. From Section 2.2 via pitch is predicted as being one of the contributing variables to temperature difference across the surface of the ISRD based on the changing contour plots observed between varying via pitch in the local model studies. Referring to Table 1.1 in Section 1.3, Zones 1 and 4 have similar via pitch values, differing only by $0.01mm$ but zones 2 and 3 have considerably different pitch values

when compared to each other. Zones 2 and 3 differ by $0.3mm$. When considering conductivity based on via density it should be expected that zones with the smallest pitch will be more conductive than a zone with a larger via pitch. Due to the location of the internal heater traces relative to the top and bottom surfaces of the ISRD, heat transfer can occur in two directions, normal and in-plane (parallel) to the ISRD surfaces. The direction of potential heat transfer can be visualized by referring to the two unit cells pictured in Figure 2.6 (Figure 2.6 not drawn to scale). Next to the isometric views are the surface area

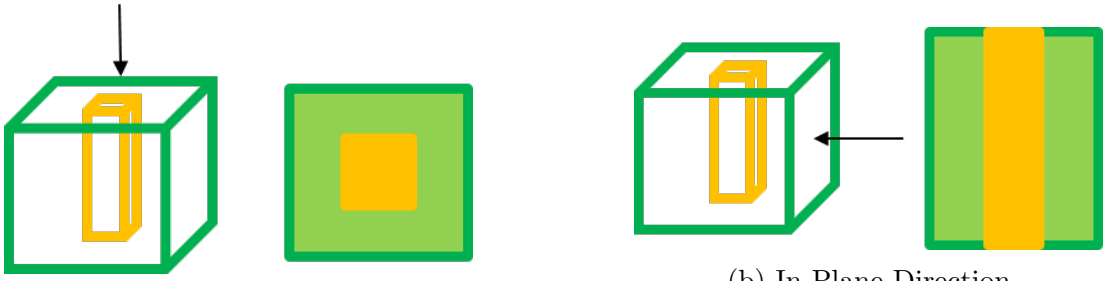

(a) Normal Direction

(b) In-Plane Direction

Figure 2.6: Normal and In-Plane Directional Heat Flow Schematics

cross-sectional views for the normal and in-plane directional heat transfer in Figure 2.6a and Figure 2.6b, respectively. The surface area views are the spatial directions through which the heat will be traveling when leaving the internal heater traces. The green material is FR-4 and the orange material is the copper vias. For the purpose of calculating the material resistance for the normal and in-plane directions of the ISRD, a heat application simplification was assumed for the unit cells. In the real ISRD the internal heater is a thin copper etching that is located $0.2032mm$ below the top surface. For the unit cells in Figure 2.6 it will be assumed that a constant heat source will cover the entire normal direction surface for the normal direction material resistance calculations, and a single heat source will cover the entire in-plane surface for the planar resistance calculations.

The normal direction spatial view of Figure 2.6a shows that when heat is applied to

the surface of the normal direction, the material resistances for copper and FR-4 should be solved in parallel. The energy leaving the heat source and traveling through the unit cell has the potential to travel through the copper and FR-4 material at the same time. The case is different for the in-plane material resistance calculation in Figure 2.6b. Since the energy must travel through the FR-4 material first, before reaching the copper via, the in-plane resistances of FR-4 and copper must be added in series.

Using the simplification to the unit cells discussed in the preceding paragraph, Figure 2.7 is presented as an example for the normal and in-plane resistance calculations performed on unit cells of the four ISRD. Unit cells from zone 2 and zone 1 are used as examples. The Zone 2 unit cell, in Figure 2.7a is from an area of low via density while the zone 1 unit cell, of Figure 2.7b is taken from a high via density region. Refer to Figure 1.4 in Section 1.3 to see the zones from which these unit cells are being studied.

The physical ISRD, is constructed of two different materials with dissimilar material properties. This study defines the composite material that most accurately captures the true conductivity of the ISRD. The equivalent material is defined as orthotropic to implement proper directional heat transfer that will take place internally within the ISRD based on the local model studies from Section 2.2. In order to calculate the resistance for the normal and in-plane directions of the two unit cells, the copper and FR-4 material were evaluated individually by employing the conductivity equation:

$$k = \left(\frac{L}{RA}\right) \tag{2.1}$$

Once the resistance and conductivity of each material form factor were found, the equivalent total resistance and conductivity were calculated to define the composite material.

Conductivity of a material is dependent on three variables: L, R, and A where L is the length along which heat travels, R is the resistivity of the material, and A is the cross-sectional surface area to which heat is applied. Comparing zone 2 and zone 1 unit cells in

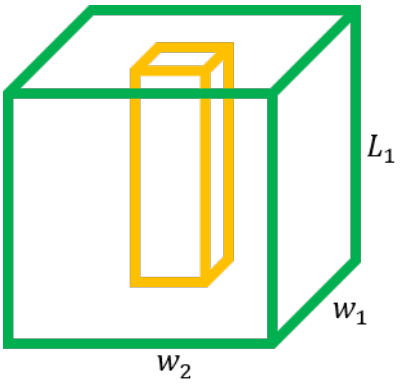

(a) Zone 2 Unit Cell Schematic

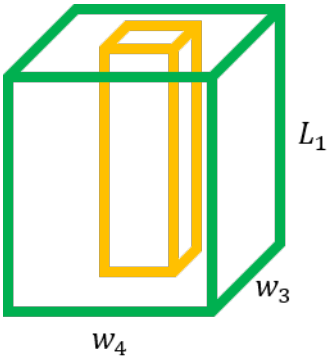

(b) Zone 1 Unit Cell Schematic

Figure 2.7: Unit Cells- Pitch and Conductivity Relationship

Figure 2.7, either the length or the surface area or both the length and surface area values will change from one unit cell to the next depending on which directional heat transfer is being considered. The FR-4 and copper material resistances will not change between the unit cells since the material types remain the same throughout the ISRD. The only two variables that will alter the conductivity value between the unit cells pictured in Figure 2.7 are L and A. When considering heat transfer in the normal direction, the surface area value will change between the two unit cells but the length value will remain the same since the L value for the unit cells are both L_1. Conversely, when heat is traveling along the in-plane direction, the length and the surface area will change from zone 2 unit cell to zone 1 unit cell. In this case, the L value in Figure 2.7b is w_2 and in Figure 2.7a it is w_4. The A value for the in-plane calculation will change as well since the w_3 edge of Zone 1 unit cell in Figure 2.7b is smaller than w_2 edge of Zone 2 unit cell.

The smaller A_{FR-4} value in zone 1 will lead to a higher conductivity value for the zone 1 unit cell as compared to the zone 2 unit cell when considering heat transfer in the normal direction. Because zone 1 has a smaller pitch and therefore a smaller A value than zone 2,

but L and R remain the same between the two unit cells, the conductivity value for zone 1 will be greater than the conductivity value for zone 2 in the normal direction. This is the basis of the prediction that the conductivity in the normal direction to the ISRD will be greater for areas of higher via density (or smaller via pitch regions).

When considering heat transfer in the in-plane direction, the length and surface area values both change between zone 2 unit cell and zone 1 unit cell. Calculating L/A for both unit cells results in the same value (1.23). Since the R does not change in any zones across the ISRD, and the L/A result does not change between zone 2 and zone 1 unit cells in Figure 2.6. The conductivity value for the in-plane direction is the same from one unit cell to the other. Therefore, it is accurate to predict that the heat transfer through the ISRD will be dominated by the differing conductivity values in the normal direction.

An example of the calculations completed for the zone 1 unit cell is presented in Equations 2.2 through 2.4. Equation 2.2 calculates the resistance for the normal direction of the copper via and the normal direction resistance of the FR-4 material.

$$\begin{aligned} R_{cu,N} &= \left(\frac{L}{K \times A_{cu,N}}\right) = \left(\frac{0.81mm}{0.385\frac{W}{mm-K} \times 0.0133mm^2}\right) \\ R_{FR4,N} &= \left(\frac{L}{K \times (A_{total,N} - A_{cu,N})}\right) = \left(\frac{0.81mm}{0.00035\frac{W}{mm-K} \times 0.627mm^2}\right) \end{aligned} \tag{2.2}$$

With both resistances calculated for the copper and FR-4 materials, the independent resistance values are summed to derive the total equivalent resistance for the unit cell. In the example of Equation 2.2, calculations are performed for the normal direction of the zone 1 unit cell, and therefore the resistances must be added in parallel. Equation 2.3 presents the equivalent normal direction resistance calculation.

$$R_{eqv,N} = \left(\frac{R_{cu,N} \times R_{FR4,N}}{R_{cu,N} + R_{FR4,N}}\right) = \left(\frac{158.6°\text{C}/W \times 3,692.6°\text{C}/W}{158.6°\text{C}/W + 3,692.6°\text{C}/W}\right) = 152.1°\text{C}/W \tag{2.3}$$

Finally, the calculated $R_{eqv,N}$ is used to solve for the equivalent conductivity in the normal direction ($k_{eqv.N}$) for the Zone 1 unit cell by using the original conductivity equation from

Equation 2.1. Equation 2.4 shows $k_{eqv,N}$ calculated to be $8.4W/m^2K$

$$k_{eqv,N} = \left(\frac{0.81mm}{(152.1°\text{C}/W) \times (0.64mm^2)} \right) \times 1,000 = 8.4W/m^2K \tag{2.4}$$

The $k_{eqv,N}$ value satisfies one direction of heat transfer within the unit cell. The in-plane equivalent resistances must be solved in order to derive the equivalent conductivity for the in-plane direction ($k_{eqv,P}$) of the unit cell. The process for deriving ($k_{eqv,P}$) is presented in Equations 2.5 through 2.7.

$$\begin{aligned} R_{cu,P} &= \left(\frac{L}{K \times A_{cu,P}} \right) = \left(\frac{0.31mm}{0.385 \frac{W}{mm-K} \times 0.011mm^2} \right) = 3.21°\text{C}/W \\ R_{FR4,P} &= \left(\frac{L}{K \times (A_{total,P} - A_{cu,P})} \right) = \left(\frac{0.8mm}{0.00035 \frac{W}{mm-K} \times 0.65mm^2} \right) = 3,527.3°\text{C}/W \end{aligned} \tag{2.5}$$

$$R_{eqv,P} = R_{cu,P} + R_{FR4_P} = 3.21°\text{C}/W + 3,527.3°\text{C}/W = 3,530.5°\text{C}/W \tag{2.6}$$

$$k_{eqv,P} = \left(\frac{0.8mm}{(3,530.5°\text{C}/W) \times (0.65mm^2)} \right) \times 1,000 = 0.35W/m^2K \tag{2.7}$$

Table 2.4 tabulates the final results of the the normal and in-plane equivalent conductivities of the unit cells for each of the four ISRD zones.

The last two columns in Table 2.4 present the calculated total equivalent conductivities for the normal and in-plane directions of the four zones within the ISRD. It's important to note that the tabulated results of Table 2.4 show the resistance values for copper in the normal and in-plane directions as unchanging. The resistance calculation is simply the conductivity equation rearranged to solve for R, and therefore it is dependent on the variables: L, K, and A. Since the via is the only structure that is made of copper in the unit cells being studied, and because the via's shape and size never changes between any of the regions within the ISRD, it stands to reason that the resistance calculations for the vias from each zone in

TABLE 2.4

Zonal Unit Cell Equivalent Conductivity Results

Zone	Resistance (°C/W)				Total Equivalent Conductivity (W/m^2K)	
	Normal		In-Plane		Normal	In-Plane
	Cu	FR-4	Cu	FR-4		
1	158.6	3692.6	3.21	3527.3	8.32	0.35
2	158.6	2345.4	3.21	3574.8	5.45	0.35
3	158.6	8647.2	3.21	3527.3	18.52	0.35
4	158.6	4854.5	3.21	3625.5	10.76	0.35

both directions will remain the same. The only value that will be changing and affecting the resulting conductivity value will be the calculated resistance of FR-4. Since the FR-4 material properties are unchanged throughout the ISRD, the change in material resistance of FR-4 is being driven by the varying size (L and A) of the FR-4 material in the unit cell. Therefore, the conductivity of the unit cells being considered are dependent upon the ratio of FR-4 material to copper material. Table 2.5 compares the relationship of pitch to the ratio of FR-4 resistance to copper resistance, and the resulting conductivity for each unit cell. With smaller via pitches and larger ratio's of FR-4 resistance to copper resistance the conductivity in the normal direction will increase.

TABLE 2.5

Zone Conductivity Relative to Fr-4/Cu Ratio

Zone	Pitch	Ratio (FR-4/Cu)	Conductivity-Normal (W/m^2K)
1	0.5	23.3	8.3
2	0.7	14.8	5.5
3	0.4	54.5	18.5
4	0.5	30.6	10.8

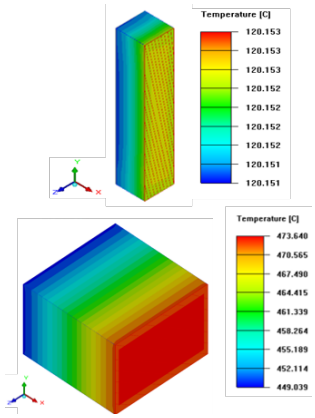

(a) In-Plane Direction

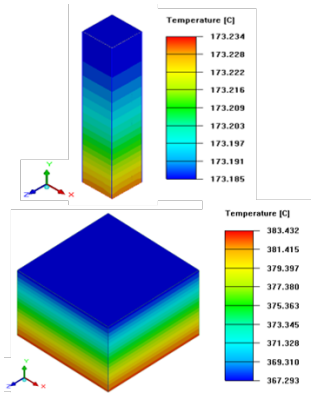

(b) Normal Direction

Figure 2.8: Analytical Conductivity Models

A computational heat transfer model of the Zone 1 unit cell was created in IcePak and found to be in good agreement with the theoretical calculations of normal and in-plane resistances completed in Equations 2.4 and 2.7, respectively. Figure 2.8 presents the computational models. The side opposite of the side with the applied power source has an arbitrary heat transfer coefficient boundary condition of $20W/m^2K$ applied. All other sides of the unit cells are set as adiabatic so the energy is forced to travel directly through the material and exit through the opposite side. This simulation was conducted as a steady state conduction only model. The beginning and ending temperatures of the unit cells were captured and the difference between the values is divided by the total amount of applied power to find the resistance of the material. Figure 2.8a shows the Zone 1 unit cell materials split apart with a heat source, of $0.007W$ of power, distributed on the X_{max} side of both the copper and FR4 material, to solve for the independent in-plane resistances of the two materials. Figure 2.8b is again the Zone 1 unit cell, but the $0.007W$ is now situated on the Y_{min} side of the separated materials to solve for the normal direction resistances.

Table 2.6 compares the simulated results with the theoretical calculations. The theoretical and computational results for FR-4 resistance compare very well and only differ by

TABLE 2.6

Theoretical vs. Computational Resistance Values

	Direction			
	Normal Resistance (C/W)		In-Plane Resistance (C/W)	
Materials	Cu	FR-4	Cu	FR-4
Theoretical	123.6	3,692.6	0.41	3,527.3
Computational	70.0	3,626.1	1.4	3,514.2
Difference	53.6	66.5	1.0	13.3

66.5°C/W and 13.3°C/W for the normal and in-plane directions, respectively. The theoretical and computational resistance results for copper in the normal and in-plane direction agree, but differ by a greater magnitude compared to the correlation of FR-4 resistance values. The resulting copper resistance value of the computational via is not considered to be a large source of error since the ratio of FR-4 to copper still remains large between the computational FR-4 and copper resistance results. The ratio between the resistances is of more importance than the absolute values.

The theoretical resistances and conductivities presented in Equations 2.2 through 2.4 lead to the reasoning for building separate heater zones into the ISRD. Since the conductivity of the different zones has been proven to be dependent on via pitch, the design scheme of the heater traces is based on via pitch as well. Four separate heater zones gives operators the ability to control each zone independently by applying more or less power in regions of higher or lower via density, respectively. Areas with higher via density will have a greater heat flux than areas with lower via density and therefore will need a larger amount of applied power to the entire region. Because the ISRD's purpose is to be able to produce heat and maintain a less than 10°C change across its top surface, it is essential to understand the conductivity characteristics in each of the four differently pitched zones and to be able to establish a relationship between the conductivity values of each zone with the corresponding

TABLE 2.7

Bulk Material Properties

Zone	Bulk Material Property Values			
	Conductivity		Density (kg/m^3)	Specific Heat
	Normal	In-Plane		
1	8.4	1.0	1390.4	1279.9
2	5.5	1.0	1390.4	1279.9
3	18.7	1.0	1390.4	1279.9
4	10.7	1.0	1390.4	1279.9

necessary power inputs.

Table 2.7 summarizes the bulk material properties that are applied to Zones 1 through 4 in the ISRD global model. The normal and in-plane equivalent values were calculated using the processes and equations presented in Equations 2.2 through 2.7. Volumetric averaging was used to derive balanced density and specific heat values for each of the zones, based on the ratio of copper content to FR-4.

There is a discrepancy between the in-plane conductivity values from Table 2.4 and Table 2.7. In Table 2.4, the in-plane conductivity values were calculated to be $0.35W/m^2K$ however, the in-plane values in Table 2.7 are shown to be $1.0W/m^2K$. The in-plane unit cell calculations of Table 2.4 were completed with the assumption that the only copper content besides the resistive heaters are the vias. However, in the physical ISRD there are additional copper resistive heater traces on the bottom internal layers. The additional heaters were built into the ISRD in order to experiment with other various heater trace routing options to combat against different variables that could drive a top surface temperature gradient across the ISRD. The investigative heater design schemes are not in the scope of this study, however it is important to understand the discrepancy between the two tables. The same calculations that were performed in the original equivalent conductivity calculations were

repeated in order to take the extra copper content into account. The resulting in-plane conductivity values from the second set of calculations for each zone resulted in $1.0 W/m^2K$ as shown in Table 2.7. The normal conductivity calculations changed by a negligible amount and therefore the second set of normal conductivity values are not captured.

2.3.4 Global Model Boundary Conditions

After calculations were completed for each block to determine appropriate size and material property assignment, the computational model was constructed in IcePak. Figure 2.9 shows an isometric view of the final computational model. The top and bottom surfaces of the ISRD are in the Y_{max} and Y_{min} directions, respectively. The outer material surrounding the ISRD internal heater traces is the extra material that houses the power pin locations. These outer blocks have been given specific material properties by utilizing the same methods of volumetric averaging and orthotropic material calculations for copper and FR-4 as described previously. The discrete blocks that define the entire ISRD structure can be observed in Figure 2.9. See Table 2.8 for each blocks geometrical properties.

TABLE 2.8: Bulk Model Block Geometry by Zone

Block Name	**X** (mm)	**Y** (mm)	**Area** (mm^2)
Zone1_block1	8.2	0.6	5.3
Zone1_block2	0.7	2.6	1.7
Zone1_block3	11.3	8.6	96.7
Zone1_block4	2.3	9.0	20.9
Zone1_block5	9.0	4.7	42.3
Zone1_block6	9.8	0.7	6.5
Zone1_block7	0.7	8.0	5.9

Table continues on next page

Continued from previous page

Zone1_block8	8.8	1.2	10.5
Zone 1 Total			189.9
Zone 2			
Block Name	X (mm)	Y (mm)	Area (mm)
Zone2_block1	13.1	11.2	146.1
Zone2_block2	29.7	2.6	78.5
Zone2_block3	6.6	8.6	56.3
Zone2_block4	4.2	13.7	58.0
Zone2_block5	2.3	4.7	10.9
Zone2_block6	16.0	4.7	74.2
Zone2_block7	28.4	1.8	50.5
Zone2_block8	9.8	6.5	63.9
Zone2_block9	6.9	10.9	74.6
Zone2_block10	5.5	3.7	20.5
Zone2_block11	2.5	1.9	4.7
Zone 2 Total Area			637.9
Zone 3			
Block Name	X (mm)	Y (mm)	Area (mm^2)
Zone3_block1	3.3	13.9	45.3
Zone3_block2	23.8	2.4	56.3
Zone3_block3	2.1	26.9	56.3
Zone3_block4	26.1	2.7	71.0
Zone3_block5	2.5	6.8	17.1
Zone 3 Area Total			246.1

Table continues on next page

Continued from previous page

Zone 4			
Block Name	X (mm)	Y (mm)	Area $(mm)
Zone4_block1	0.6	22.1	12.6
Zone4_block2	3.3	3.6	11.9
Zone4_block3	6.3	2.4	14.9
Zone4_block4	36.9	0.7	24.0
Zone4_block5	6.2	2.4	14.7
Zone4_block6	3.3	2.6	8.7
Zone4_block7	0.7	36.8	24.3
Zone4_block8	3.2	3.9	12.6
Zone4_block9	2.3	2.1	4.8
Zone4_block10	34.3	0.6	22.0
Zone4_block11	2.7	3.9	10.7
Zone4_block12	6.8	2.5	16.9
Zone 4 Total Area			178.2
Grand Total Area			1251.9

The thickness of each block in the Y direction within the model is set at $0.8128mm$, the same thickness as the actual ISRD. All blocks in the bulk conduction model are assigned their respective zone equivalent material properties calculated in Section 2.3.3 and summarized in Table 2.7.

Since the focus of this study is only the surface temperature of the ISRD, radiation is turned on and the model is assumed to be radiating to just the surrounding ambient air. For this thesis, the model is evaluated exclusively as a steady state conduction simulation. Each block that makes up the ISRD is specified as a conducting solid. Icepak treats the

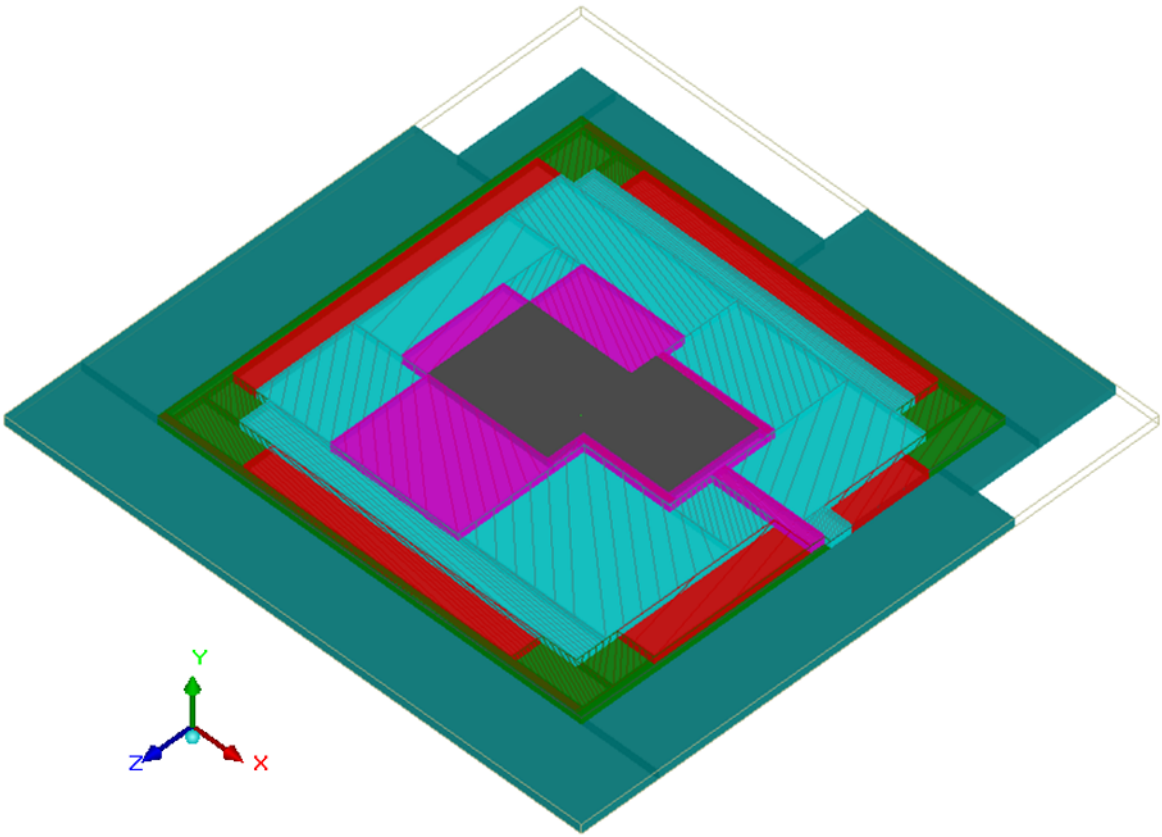

Figure 2.9: Computational ISRD Bulk Model

ISRD global model as a singular block, ignoring the contact resistance between the discrete blocks that construct the model. External convection heat transfer coefficients are applied to all surfaces of the ISRD. The convective heat transfer coefficients were calculated by utilizing the Rayleigh number and Nusselt number empirical correlation equations. Because the purpose of the ISRD is to reach extreme temperatures in order to simulate a thermal solution failure within a high powered system, it would be counterproductive to have applied forced convection heat transfer. The only external convective heat transfer that is present during computational simulations and experimental trials is natural free convection.

Rayleigh and Nusselt numbers are two dimensionless numbers that work well as empirical correlations to estimate the convective heat transfer due to buoyancy driven flows of a fluid.[8]

In the case of this study, the fluid under consideration is normal compressible air. The ISRD simulation study assumes ambient air to be 20°C at the beginning of each trial run. The equation to derive the average heat transfer coefficient is expressed as[8]:

$$\overline{h_s} = \left(\frac{k}{L}\right)\overline{Nu_L} \tag{2.8}$$

where $\overline{h_s}$ is the average surface convection coefficient and $\overline{Nu_L}$ is the dimensionless Nusselt number. In order to calculate the Nusselt number which is necessary for use in the convective heat transfer coefficient equation, the Rayleigh number equation is employed and is expressed as[8]:

$$\overline{Ra_L} = \frac{g\beta\left(T_s + T_\infty\right)L^3}{\nu\alpha} \tag{2.9}$$

where g is gravity, β is film temperature, T_s is surface temperature of the object in question, T_∞ is the ambient temperature, L is the characteristic length of the object, ν is kinematic viscosity and α is thermal diffusivity. For the Rayleigh equation, each of the air properties are calculated at the film temperature. Therefore, the Rayleigh number is dependent upon the difference between the surface and ambient temperature as well as the size of the object. It should be expected that with differing surface and ambient temperatures as well as with differing length values the external heat transfer coefficient will change.

Once the Rayleigh number is calculated, the next step is to calculate the Nusselt number. The empirical correlation for the use of Nusselt number in the calculation of the average surface convection heat transfer coefficient from the upper surface of a hot plate or Lower Surface of a cold plate[8]:

$$\begin{aligned} \overline{Nu_L} &= 0.54\overline{Ra_L}^{1/4} \\ for &: \left(10^4 < \overline{Ra_L} < 10^7, Pr > 0.7\right) \end{aligned} \tag{2.10}$$

For the bottom surface of a horizontal hot plate the empirical correlation for the use of Nusselt number in the calculation of the average surface convection heat transfer coefficient

is[8]:

$$\overline{Nu_L} = 0.52\overline{Ra_L}^{1/5}$$
$$for : (10^4 < \overline{Ra_L} < 10^9, Pr > 0.7) \tag{2.11}$$

The Nusselt number is directly dependent on the Rayleigh number. As the Rayleigh number changes so does the Nusselt number. Certain Nusselt number equations can only be used depending on if they meet the criteria for the direction of heat transfer and if the Rayleigh number falls within a certain value. The criteria for Nusselt number usage is summarized in Equations 2.10 and 2.11. The Rayleigh number is solved by considering the surface temperature (T_s) of the ISRD and the ambient temperature(T_∞) of the surrounding air. From the surface and ambient temperature the film temperature (T_f) can be found. The film temperature is the arithmetic mean of the T_s and T_∞ temperatures and is the value at which the air properties are used for input to the Rayleigh equation. The thermal diffusivity (α), kinematic viscosity (ν), and conductivity (k) are all evaluated for air at the calculated T_f temperature. L is simply the characteristic length of the surface. For purposes of solving the Rayleigh number in terms of the ISRD. The ISRD surface area is divided by the perimeter for a value of $0.0014mm^2$. Once all variables have been calculated, the Rayleigh number can be equated. The Rayleigh number is then used to solve for Equation 2.10 or Equation **??** depending on which direction the hot surface is facing. The resulting convection coefficients for each wall direction and maximum temperature point are summarized in Table 2.11.

In order to calculate the average heat transfer coefficient, the air properties from Table 2.9[8] must be calculated for use in the Rayleigh number calculation. Since the Rayleigh number is evaluated at the film temperature, (T_f), then the surface and ambient temperature must be understood to properly calculate the correct Ra. The correlation plan will be described in later chapters, but for the example to be shown here, it will be stated that the first correlation temperature will be 100°C. The surface temperature of the ISRD is expected to reach 100°Cin the first computational single zone trial. A double interpolation can be

performed on the air properties from Table 2.9 in order to determine the correct values at to solve the film temperatures for use in the Rayleigh equation.

TABLE 2.9

Compressible Air Properties from $300K$ to $400K$

Temperature (K)	α $(m^2 \times 10^6)$	ν $(m^2/s \times 10^6)$	k $(W/mK \times 10^3)$	Pr
300	22.5	15.9	26.3	0.71
350	29.9	20.9	30	0.71
400	38.3	26.4	33.8	0.69

To accurately calculate the air properties at the temperatures of interest, information from Table 2.9 is utilized for use in the double interpolation in Equation 2.12:

$$y = y_1 + (y_2 - y_1) \times \left(\frac{x - x_1}{x_2 - x_1} \right) \tag{2.12}$$

For example, air properties at the T_f temperature 60°C ($333.15K$) are of interest since that is the arithmetic mean of ambient temperature at 20°C and a surface temperature of 100°C. Equation 2.13 is an example calculation completed to interpolate the value of thermal diffusivity (α) at a T_f temperature of 60°C (333.15), by using the known air properties at the $300K$ and $350K$.

$$\begin{aligned} y &= 22.5 \times 10^6(m^2) + \left(29.9 \times 10^6(m^2) - 22.5 \times 10^6(m^2)\right) \times \left(\frac{333.15K - 350K}{350K - 300K} \right) \\ y &= 27.4 \times 10^6(m^2) \end{aligned} \tag{2.13}$$

Solving for y results in the interpolated value of thermal diffusivity that should be used for the calculation of $\overline{Ra_L}$ at the T_f of 60°C.

The correlation temperatures of the ISRD will be between 100°C and 250°C, therefore, with an ambient temperature of 20°C, the T_f temperatures for which the average surface convection heat transfer coefficient will be solved for will fall between the values between 60°C and 135°C. The air properties at these temperatures are of most interest in order to

TABLE 2.10

Interpolated Air Properties

Temperature (°C)	α $(m^2 \times 10^6)$	ν $(m^2 \times 10^6)$	k $(W/mK \times 10^3)$	Pr
60	24.5	17.2	27.3	0.71
85	28.2	19.7	29.1	0.70
110	32.1	22.2	30.1	0.70
135	36.3	24.8	32.8	0.70

solve the theoretical heat transfer coefficient for application as a boundary condition to the computational bulk model. Using the double interpolation calculation from Equation 2.12, and the known properties of air at $300K$, $350K$, and $400K$, the following air properties were calculated at the T_f for each maximum temperature point (60°C, 85°C, 110°C, and 135°C) and summarized in Table 2.10. The Rayleigh number is calculated for each of the four temperature points. Based on the result of the Rayleigh number, a specific Nusselt equation was used to calculate the dimensionless Nusselt number which is then finally used to calculate the external heat transfer coefficient. Table 2.11 summarizes the resulting average convection coefficients used as external boundary conditions the bulk computational ISRD model.

TABLE 2.11

Average Surface Convection Coefficients

Cabinet Wall	Temperature (°C)	Calculated Coefficient (W/m^2K)
Min-Y	100	2.5
	150	2.8
	200	3.1
	250	3.3
Max-Y	100	2.6
	150	2.9
	200	3.2
	250	3.4
Max-Z	100	3.9
	150	4.1
	200	4.2
	250	4.3
Min-Z	100	3.9
	150	4.1
	200	4.1
	250	4.2
Max-X	100	3.8
	150	4.0
	200	4.1
	250	4.2
Min-X	100	3.8
	150	4.0
	200	4.1
	250	4.2

CHAPTER 3

Experimental Trials

3.1 Experimental Set up

To aide in the thermal analysis study, preliminary experiments were performed on the ISRD in order to provide experimental data for the simulation to use as correlation points. The data used for correlation was provided in the form of thermal images obtained by using a FLIR thermal imaging camera. A schematic of the experimental set up is shown in Figure 3.1.

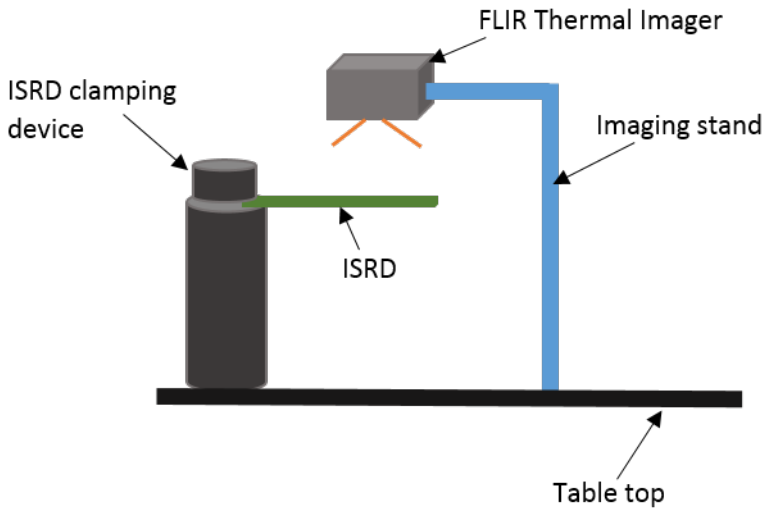

Figure 3.1: Schematic of Laboratory Set up

The ISRD clamping device was a simple fixture that was used to hold the edge of the ISRD so the entire heater trace region was floating in air. This was an important requirement

for the experimental set up, to avoid any heat sinking from objects that the ISRD would have otherwise been resting on during trial runs. By setting up the experiments so the ISRD was freely floating in air, the thermal model could easily copy this simulation by setting the surrounding cabinet walls to be boundaries to ambient air. The FLIR camera was assembled on its stand so that it was hovering directly over the ISRD heater trace region. Since this study was not concerned about what was happening in the outer regions where the power pins are positioned, it was only critical to have the FLIR imager capture the entire heater trace region, so the thermal contour plots in this area could be studied.

Since the ISRD has four heater zones, each of the heater zones were tested individually at four different temperature points in order to gather enough data about surface temperature behavior and power input to compare with the computational simulation. Four temperature points were chosen to simulate the peak temperatures that occur during a solder reflow profile, for reasons discussed in Section 1.2.1. The temperatures of 100°C, 150°C, 200°C, and 250°C are referred to as the "probe points" that were considered in the experiments. Each of the four heater zones within the ISRD were powered on and supplied with an appropriate amount of power (W) to achieve each of the four desired temperature probe points. The voltage and current were manually operated to achieve the necessary wattage to attain the four separate probe points. For each probe point, the ISRD took approximately thirty minutes to reach steady state. Once steady state was achieved, an ISRD image was captured and stored along with the image. After each probe point temperature was captured, the ISRD was allowed to cool back to room temperature before beginning the next probe point ramp.

After thermal images were captured in the laboratory, the data was uploaded to a folder which could be accessed by the FLIR imaging software. The FLIR imaging software is an interactive service in which images can be altered and manipulated to extract pertinent data for the study. In areas of interest, surface temperature probes were applied to the ISRD thermal images for later comparison with the results from the computational analysis.

Between eight and eleven probe points were applied to each thermal image. The temper-

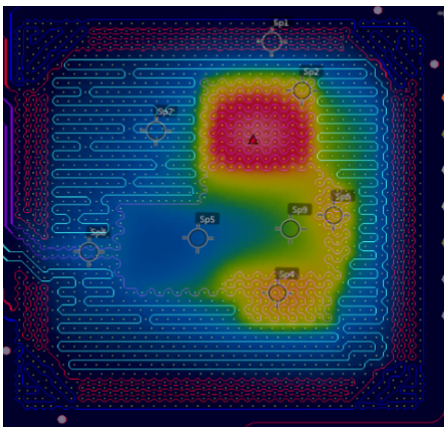

(a) Zone 1 Exp. Probe Points

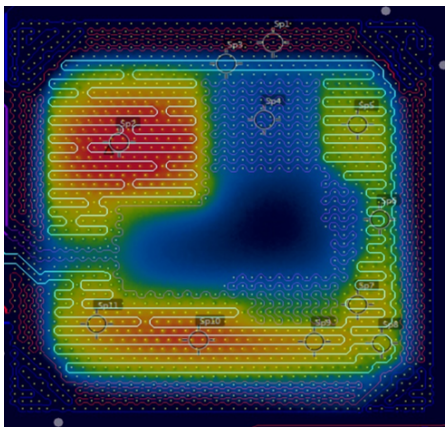

(b) Zone 2 Exp. Probe Points

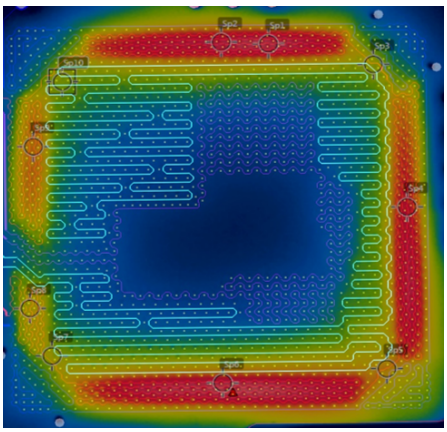

(c) Zone 3 Exp. Probe Points

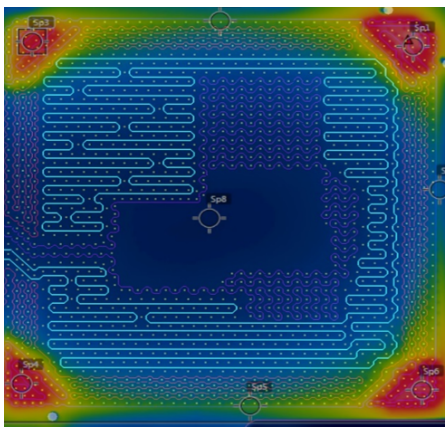

(d) Zone 4 Exp. Probe Points

Figure 3.2: Experimental Probe Point Locations

ature points applied in the FLIR images focused on areas of transition between the heated zone and the adjacent cool zones. By focusing on these transition areas, the heat transfer between the powered and non powered zones and parallel variables such as via density, heater location relative to external ISRD material, can be considered. The temperature points also focused on hot and cold spots within the single zones. By considering the hot spots and cold spots, this will give us a baseline comparison of how well the heater traces within a single

zone are balanced.

To compare the images, surface probe points were established on the thermal images using the FLIR imaging software. Overlay images of the heater trace routing and the thermal images were created in order to help pin point the exact location of where to apply surface probes in the thermal model. The thermal overlay plots can be found in Figure 3.2.

In addition to the single heater zone experimental trials, a separate experiment was also completed to study the effect of all heater zones powered on simultaneously. The same approach from the single heater studies was used to compile data from the simultaneous zone study. The same four probe point temperatures were achieved by tuning the voltage and current input to each heater zone. FLIR images were once again captured and stored for later correlation to theoretical models. All results from the single and simultaneous experiments will be discussed in the following section of this chapter.

3.2 Experimental Results

The experimental results discussed in this section are essential to the success of this study, as they are the primary data that is used for correlation of the ISRD computational model. The results from the experimental part of this study are presented in this section. Each of the four heater traces was powered to each of the four probe point temperatures, resulting in a total of 16 data points for direct comparison to the computational model. Figure 3.3 through Figure 3.6 present the four probe point temperature data for each of the single zone studies.

As was seen in the computational models, the contour plots do not change from one probe point temperature to the next. The only observable change between the different probe point temperatures for a single zone study is the absolute temperature scale. The absolute temperatures increase, but the contour plots and gradients observable within a single zone as well as across the surface of the ISRD remain the same.

Figure 3.3 presents the experimental contour plots for the Zone 1 single zone study.

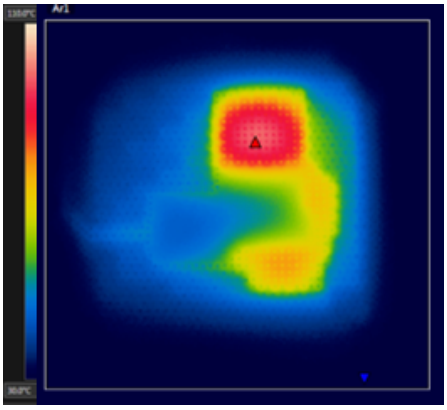

(a) Zone 1 100°C Result

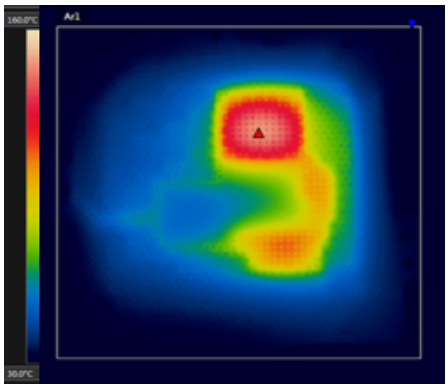

(b) Zone 1 150°C Result

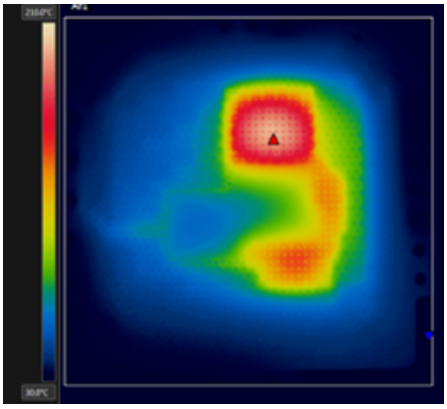

(c) Zone 1 200°C Result

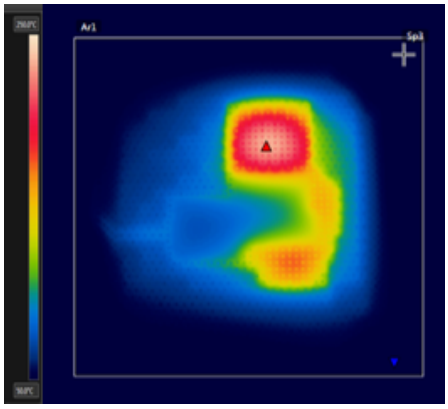

(d) Zone 1 250°C Result

Figure 3.3: Zone 1 Experimental Results

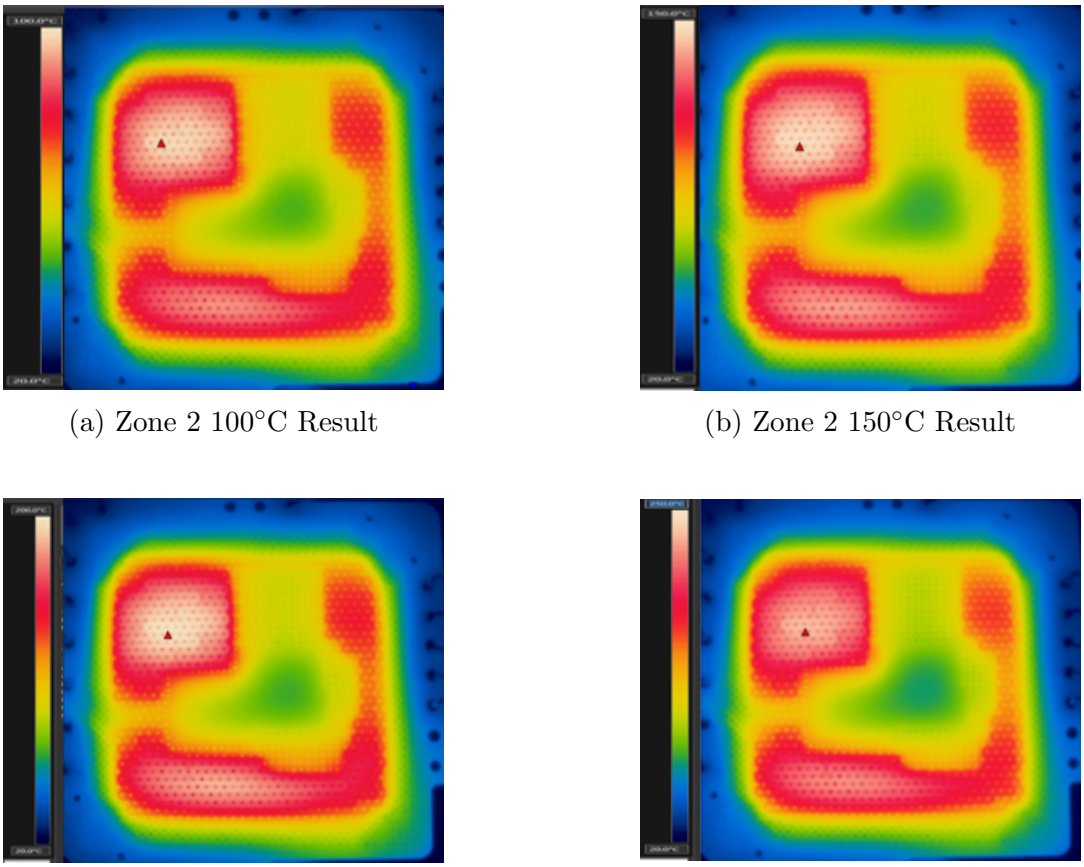

(a) Zone 2 100°C Result

(b) Zone 2 150°C Result

(c) Zone 2 200°C Result

(d) Zone 2 250°C Result

Figure 3.4: Zone 2 Experimental Results

Thermal and power data was captured for each of the four temperature probe points from 100°Cto 250°C. The change in contour plots between each of the four temperature probe points is minimal. However, the absolute temperatures change drastically between each of the probe points as would be expected. The results for the Zones 2 through 3, presented in Figures 3.4 through 3.6 are similar to Zone 1; the contour plot change is minimal but the absolute temperatures are elevated as the power level is increased.

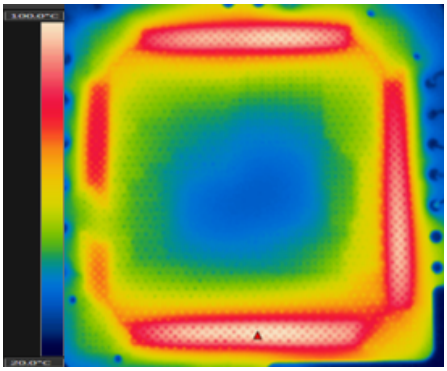

(a) Zone 3 100°C Result

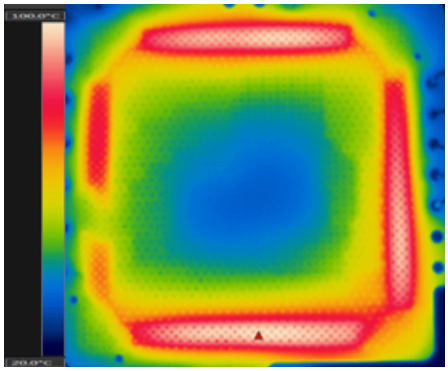

(b) Zone 3 150°C Result

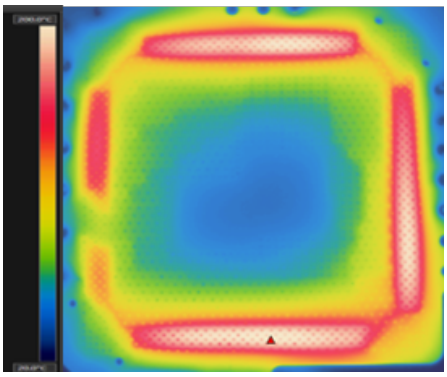

(c) Zone 3 200°C Result

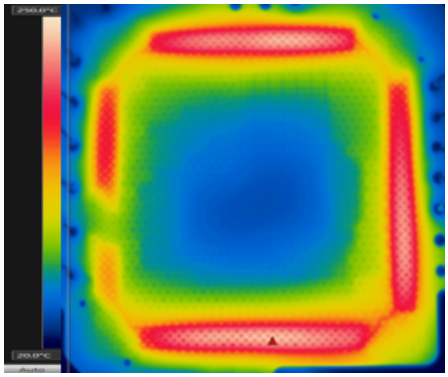

(d) Zone 3 250°C Result

Figure 3.5: Zone 3 Experimental Results

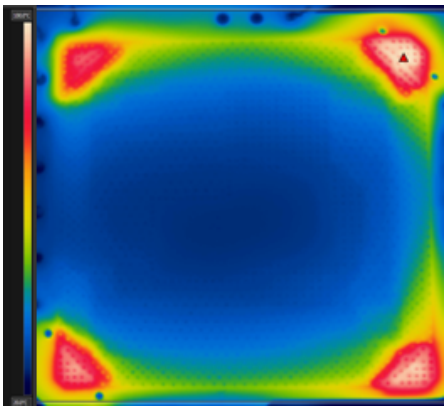

(a) Zone 4 100°C Result

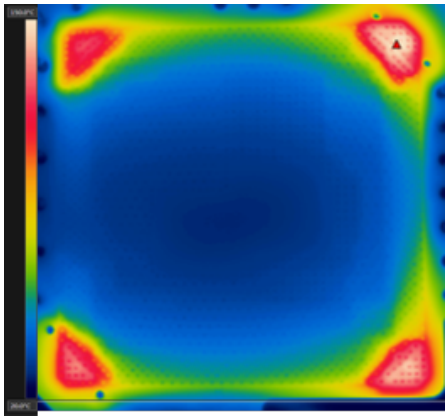

(b) Zone 4 150°C Result

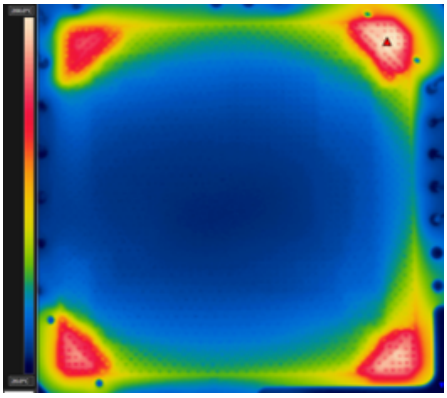

(c) Zone 4 200°C Result

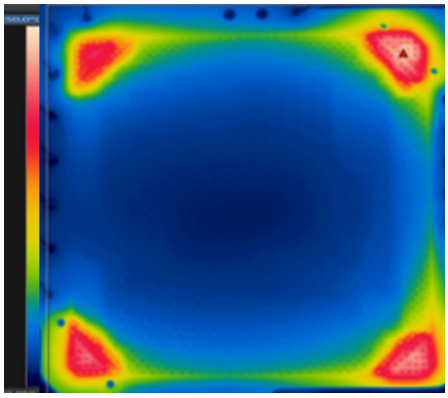

(d) Zone 4 250°C Result

Figure 3.6: Zone 4 Experimental Results

CHAPTER 4

Computational Simulations

This chapter presents a discussion on the runs of the thermal analysis study completed on the computational bulk global ISRD model. The heat transfer coefficients, material properties, and boundary conditions applied to each trial run have been calculated using the processes described in Section 2.3.

The first computational studies evaluated singular zones for direct comparison to the laboratory data of the singular heater trace studies completed previously. Laboratory power data from each of the singular zone studies was applied to the respective corresponding single zones in the computational models. As a single heater zone was being analyzed, all other heater zones were left at zero power input. Once the results from the analysis were complete, the experimental data and computational results were compared. Correlation accuracy between the experimental and computational studies will be discussed in Chapter 5.

The computational singular zone study process was conducted in the same manner as the experimental singular zone studies in Section3.2. The parameters and boundary conditions discussed in Section 2.3 were applied to each computational iteration, depending on the heater zone and the temperature point to be studied. Each model was conducted as a steady state iteration. After the solver converged, thermal contour plots were the output for each of the six sides of the ISRD global model. The focus of this thesis is to observe the temperature gradients across the Y_{max} surface of the ISRD, therefore all results presented in this section show the Y_{max} surface. Since there are four zones and four temperature

points the total number of experimental and computational singular zone trials completed total 32: 16 experimental trials and 16 computational trials. Four additional experimental and computational trials were completed, at each of the temperature points, for all zones turned on with corresponding power data applied. A grand total of 40 experimental and computational trials were completed.

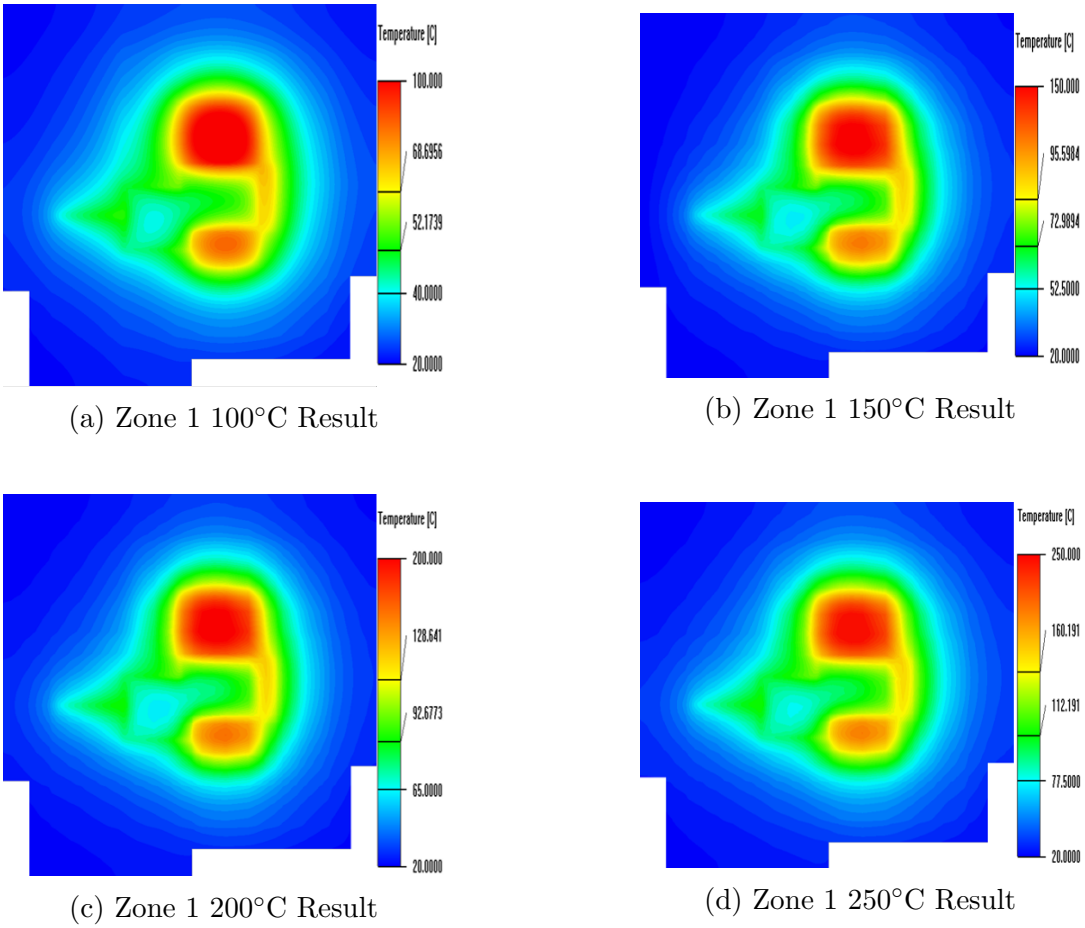

(a) Zone 1 100°C Result

(b) Zone 1 150°C Result

(c) Zone 1 200°C Result

(d) Zone 1 250°C Result

Figure 4.1: Zone 1 Computational Results

Figure 4.1 presents the Zone 1 singular zone computational results. The contour plots show minimal change between the four maximum temperature points that were simulated. The only significant change observable between the computational results at each of the maximum temperature points is the absolute temperature change. As power is increased, the

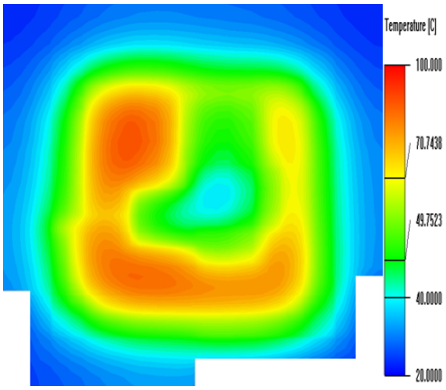

(a) Zone 2 100°C Result

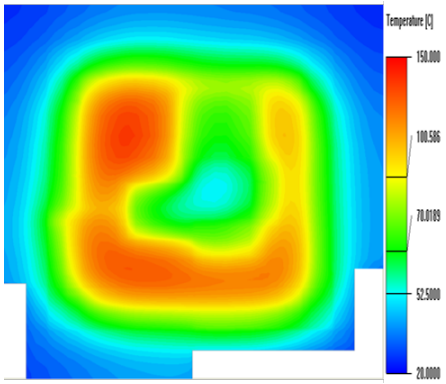

(b) Zone 2 150°C Result

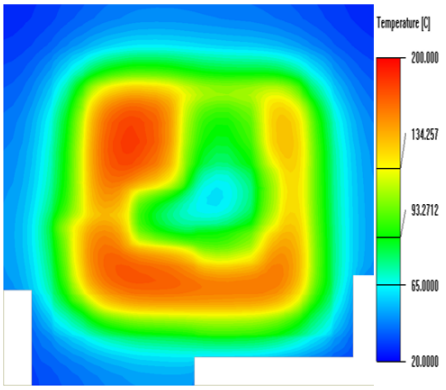

(c) Zone 2 200°C Result

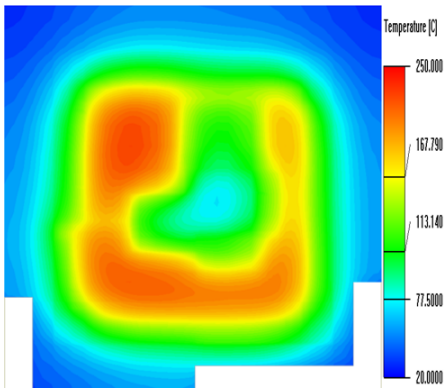

(d) Zone 2 250°C Result

Figure 4.2: Zone 2 Computational Results

absolute temperature of the overall ISRD increases as well. The stabilized contour plots is an expected outcome. Since the internal material of the ISRD is unchanging, the conductivity of the ISRD will remain unchanged as well. Therefore the internal heat flux of the ISRD will remain stable and the contour plots will look the same from one maximum temperature trial to the next. It is also expected that the absolute temperatures will continue to rise, as additional power is applied to the zones. An increased amount of power is applied to the same zone area, therefore the density of power will increase which leads to an elevated surface temperature as compared to the previous correlation trial temperature. Zones 2 through 3 presented in Figures 4.2 through 4.4 show similar outcomes as the Zone 1 computational

results.

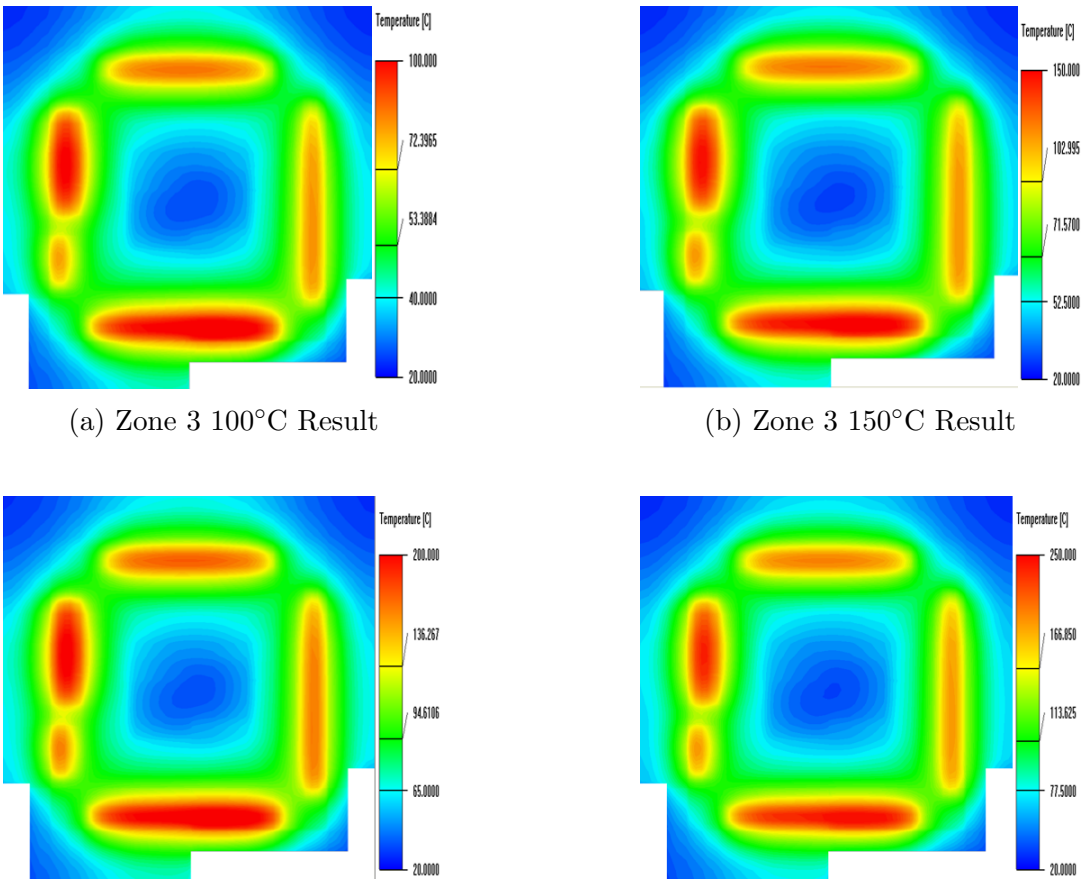

(a) Zone 3 100°C Result

(b) Zone 3 150°C Result

(c) Zone 3 200°C Result

(d) Zone 3 250°C Result

Figure 4.3: Zone 3 Computational Results

Another observation of interest is the thermal gradient across the Zone 1 area. It is expected to see large thermal gradients across the entire ISRD surface during singular zone studies, however the thermal gradients within just the single zone areas should be noted. In the north region of Zone 1 there is a large hot spot as compared to the rest of the Zone 1 regions. This hot spot occurs because this is the area of most power density, as half of the heater traces that occupy Zone 1 run through this region. From Table 2.8, z1-block3 inhabits a surface area of $96.7mm^2$ of a total Zone 1 surface area of $189.9mm^2$. Z1-block3 therefore inhabits 50% of the total Zone 1 surface area and 50% of all power applied Zone 1

during maximum temperature trials will be applied to that region.

For the Zone 2, results presented in Figure 4.2 show that the Zone is thermally unbalanced, for similar reasons as Zone 1. The north region is cooler than the the south region and the west region is cooler than the east region. Referring to Figure 2.5 the cold spots are occurring because the heater geometry within Zone 2 is not symmetrical. In other words, the south and east regions have a more equally distributed amount of heater zone area as compared to the west and north regions. An unbalanced heater zone shape seems to have an effect on the gradients within Zone 2. The same observation can be made for the north most region of Zone 2.

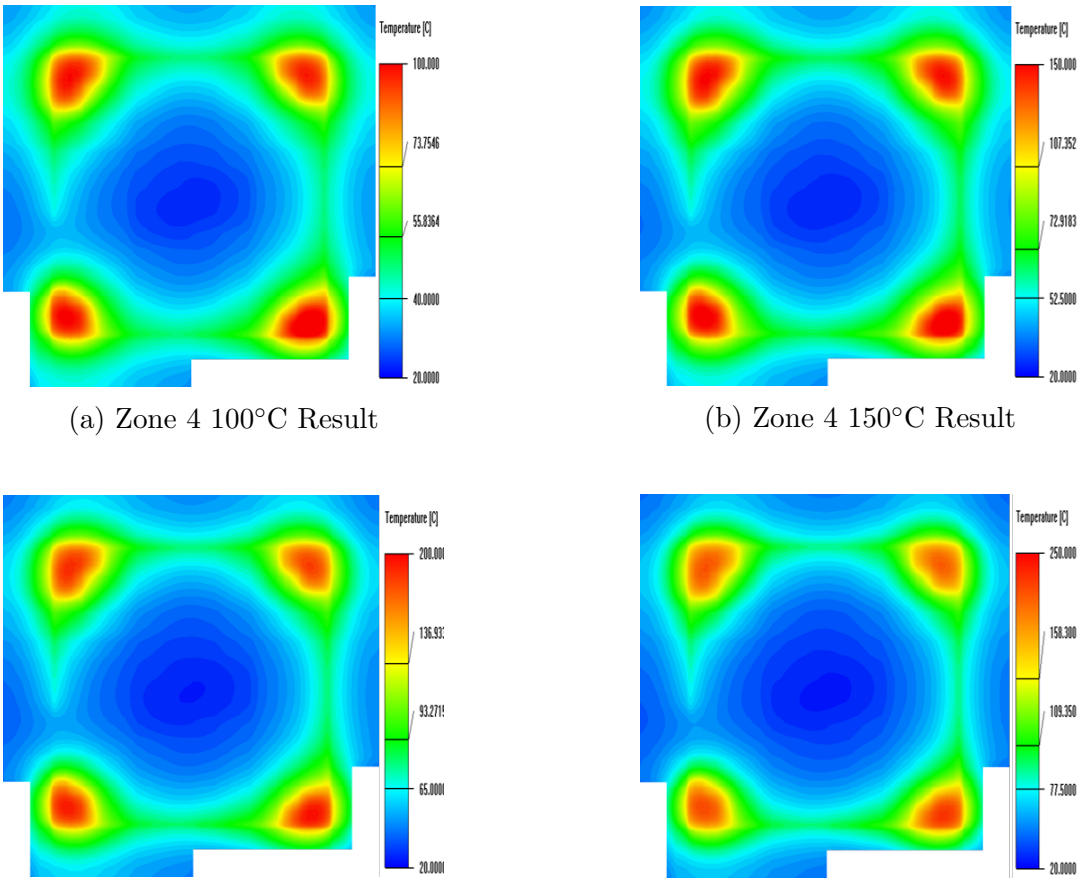

(a) Zone 4 100°C Result

(b) Zone 4 150°C Result

(c) Zone 4 200°C Result

(d) Zone 4 250°C Result

Figure 4.4: Zone 4 Computational Results

Figure 4.3 shows the computational results of the singular zone study for Zone 3. Again, zone specific temperature gradients can be observed in areas of high power density versus low power density. Between each of the major edges of zone 3 there are small single heater traces that connect the major edges. (The single traces can be observed in Figure 2.5). There is minimal power being applied to the interstitial spaces between the major edges of Zone 3 and therefore this Zone appears to have the largest zone specific thermal gradients. Similar to Zone 3, Zone 4 heater trace design also has a single trace connecting each of the four corners. The contour plots presented in Figure 4.4 shows that the four corners of Zone 4 heat up relatively consistently however, the exterior edges connecting the four zones are significantly cooler.

CHAPTER 5

Comparison

Contour plot results from the experimental and computational singular zone studies have been presented in Chapters 3 and 4. The data from these studies will be presented side by side in this chapter to study the absolute temperature comparison at specified probe points within each zone. Figure 5.1 shows the location of the probe points established in the computational model for temperature comparison agains the temperature at the corresponding location in the experimental single zone studies. Refer to Figure 3.2 in Chapter 3 to see the thermal overlay plots with the corresponding probe point locations in the experimental studies.

Figure 5.2 compares the computational results for Zone 1 at the maximum temperature point 100°C, against the experimental contour plot at the same maximum temperature point. As discussed in Chapter 4, the contour plots appear to be in good agreement. The contour plot results for the remaining maximum temperature points (150°C, 200°C, and 250°C) in the singular Zone 1 study are presented in Figure 1 of Appendix 6.3. The computational contour plots at 150°C, 200°C, and 250°C for the Zone 1 singular study are also in good agreement with the experimental contour plots.

However, when comparing the absolute temperatures of the computational results to the experimental data, there is an offset. Figure 5.3 is a graphical comparison of each computational probe point temperature compared to its' corresponding experimental probe point. Temperature is plotted on the vertical axis of each graph, and the probe point location

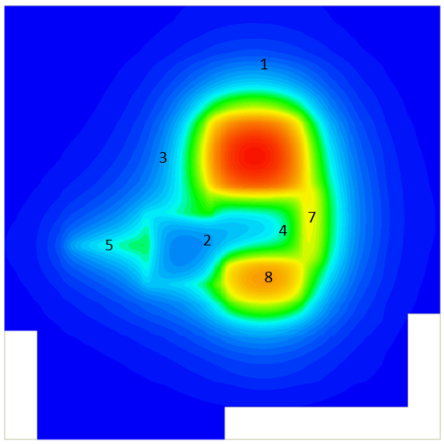

(a) Zone 1 Computational Probe Points

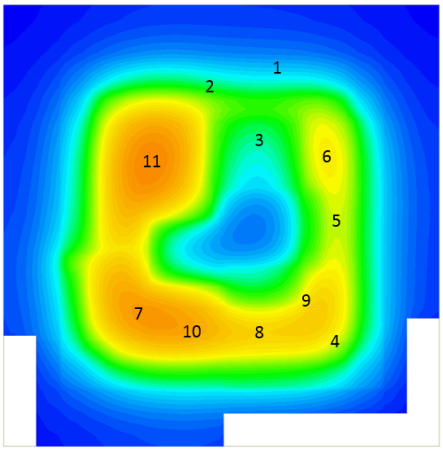

(b) Zone 2 Computational Probe Points

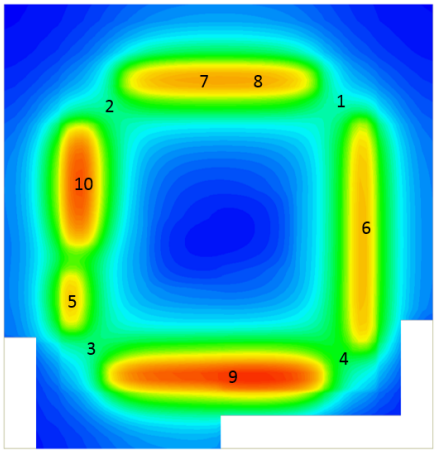

(c) Zone 3 Computational Probe Points

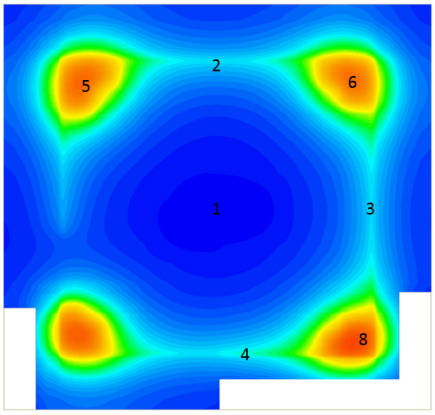

(d) Zone 4 Computational Probe Points

Figure 5.1: Location of Single Zone Computational Probe Points

number is plotted on the horizontal axis. Refer to Figure 5.1 to identify the location of each probe point within it's respective zone.

In Figure 5.3a, the Zone 1 probe points at the 100°C maximum temperature point consistently under predict the local temperature values as compared to experimental temperatures at the corresponding probe points. The exceptions are probe points numbers 5 and 8, which more closely predict the absolute temperatures at those particular probe point locations.

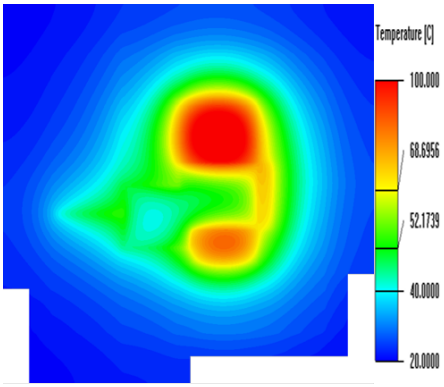

(a) Zone 1 100°C- Computational

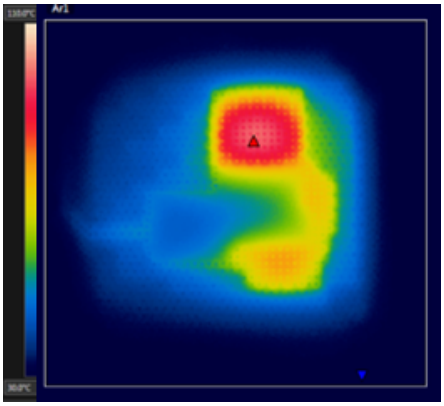

(b) Zone 1 100°C-Experimental

Figure 5.2: Zone 1, 100°C Temperature Point Comparison

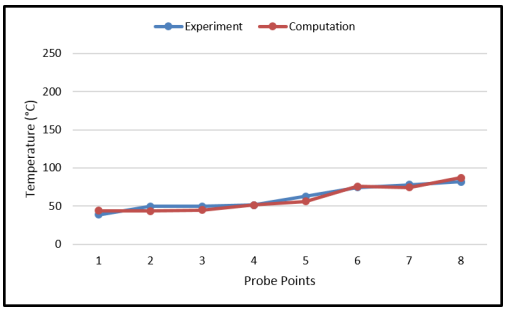

(a) 100°C Max. Temp. Probe Point Comparison

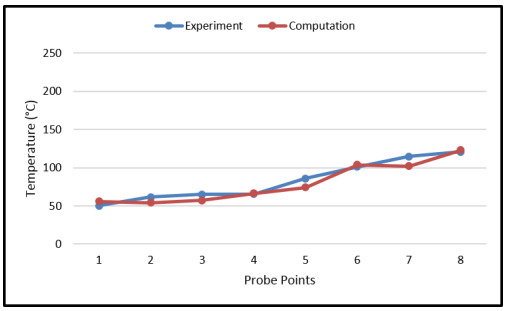

(b) 150°C Max. Temp. Probe Point Comparison

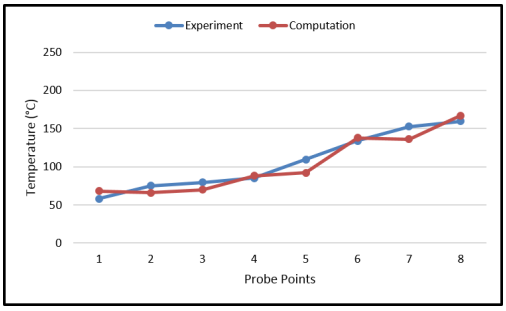

(c) 200°C Max. Temp. Probe Point Comparison

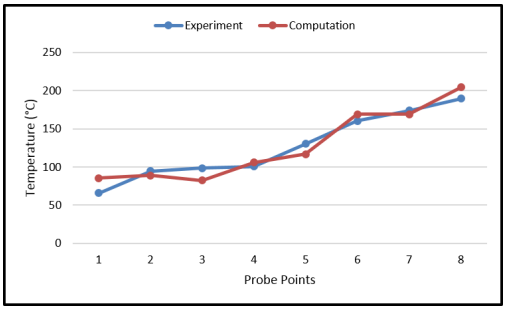

(d) 250 °CMax. Temp. Probe Point Comparison

Figure 5.3: Zone 1 Probe Point Comparison

Figures 5.3b through 5.3d show that as the maximum temperature point within Zone 1 is increased during the subsequent trials, the computational probe points continue to under predict the absolute temperature values captured in experimental results. The offset between computational temperature results and experimental data continues to increase as the maximum temperature is elevated.

The variation in offset of each probe point within Zone 1, from the beginning maximum temperature point (100°C) to the final maximum temperature point (250°C) can be observed in the bar graph of Figure 5.4. Figure 5.4 highlights that the computational model either slightly over predicts or under predicts the absolute temperatures at certain probe points. However, the offset of the computational model as compared to experimental data doesn't increase as the maximum temperature point increases. There is no clear pattern observed in terms of offset between absolute temperatures. The bars displayed in Figure 5.4 are the

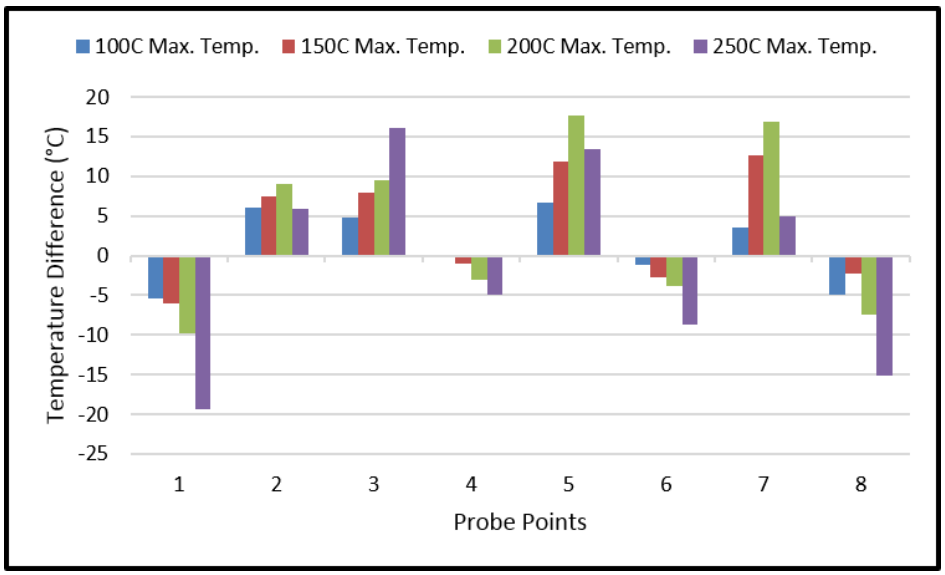

Figure 5.4: Zone 1 Absolute Temperature Offset Comparison

resulting values of the computational probe point temperatures subtracted from their corresponding experimental probe point temperatures. Therefore a positive bar value indicates at a specific probe point location, the computational model is under predicting the absolute

temperature value when compared to the experimental temperature value. A negative bar value would indicate the opposite, that the computational model is over predicting the probe point temperature.

At the 100°C maximum temperature point trial (displayed as the blue bars in Figure 5.4), the absolute temperatures of each computational probe point are predicting the absolute temperature within 7°C of the experimental temperature probe points. At the 150°C maximum temperature trial (represented by the red bars) the computational model predicts each probe point within 13°C. At the 200°C maximum temperature point (green bars) the absolute temperatures are predicted within 17°C. And at the final maximum temperature trial, 250°C(represented by the purple bars) the largest offset can be observed at probe point 1 which is showing an offset of 19°C. Although at some probe points, the computational model is over predicting and at other points it is under predicting, for zone 1 the computational model is consistently predicting the absolute temperatures within 20°C.

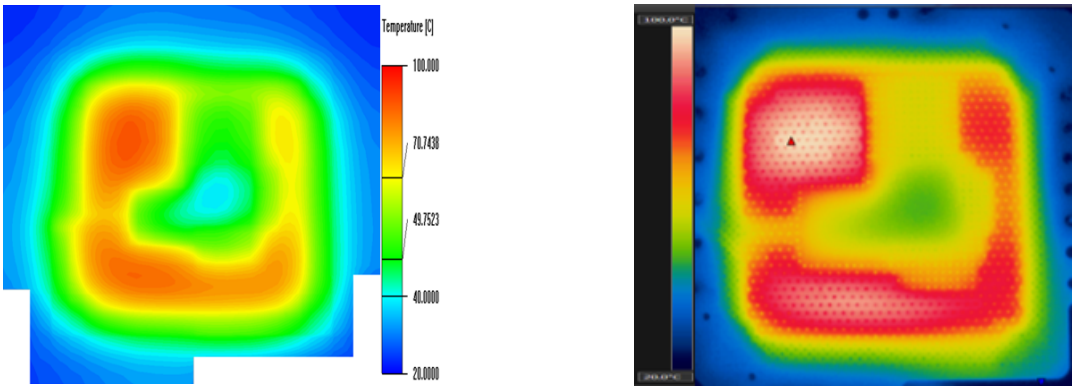

(a) Zone 2 100°C- Computational

(b) Zone 2 100°C-Experimental

Figure 5.5: Zone 2 Single Heater Computational vs. Experimental Contour Plots (100°C)

Zones 2, 3, and 4 show similar results to Zone 1. All computational contour plots for the remaining zones are in good agreement with the respective experimental contour plots for the corresponding zone trials. However, in each singular zone study, the majority of

computational probe points continue to result in values which either are slightly over or under predicting the absolute values seen in experimentation. Figure 5.5 presents the computational contour plots and the experimental contours at the 100°C maximum temperature point of the Zone 2 singular trial. The contour plots for the remaining maximum temperature points in the zone 2 single trace study can be found in Figure 2 of Appendix A. Figure 5.6 compares the computational versus experimental probe point temperatures within Zone 2.

Similarly to Figure 5.3, the Zone 2 computational probe point temperatures and the

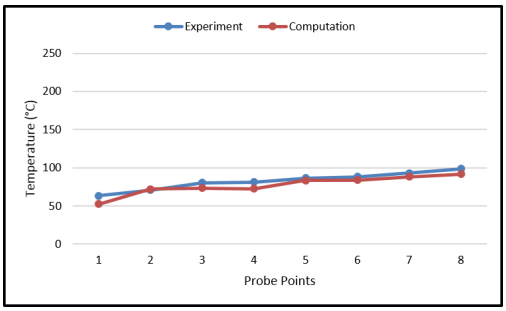

(a) 100°C Max. Temp. Probe Point Comparison

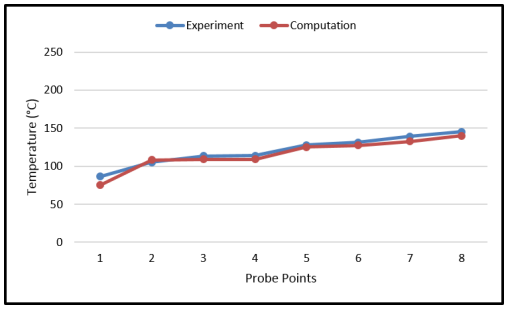

(b) 150°C Max. Temp. Probe Point Comparison

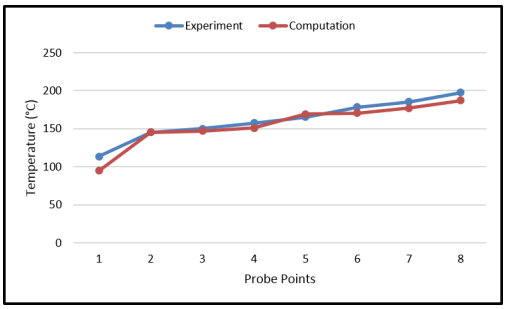

(c) 200°C Max. Temp. Probe Point Comparison

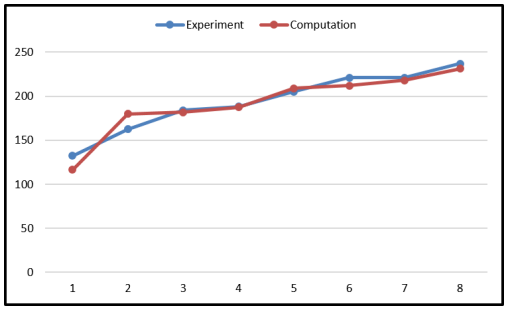

(d) 250 °CMax. Temp. Probe Point Comparison

Figure 5.6: Zone 2 Probe Point Comparison

experimental probe point temperatures in Figure 5.7 agree well. Referring to Figure 5.7 the offset between all probe points with the exception of probe point 1, are at or below a 10°C offset. Probe point 1 in Zone 2 comparative study is placed in a region of high heat flux (see Figure 5.1c for point 1 location), and this could be a contributing factor for the

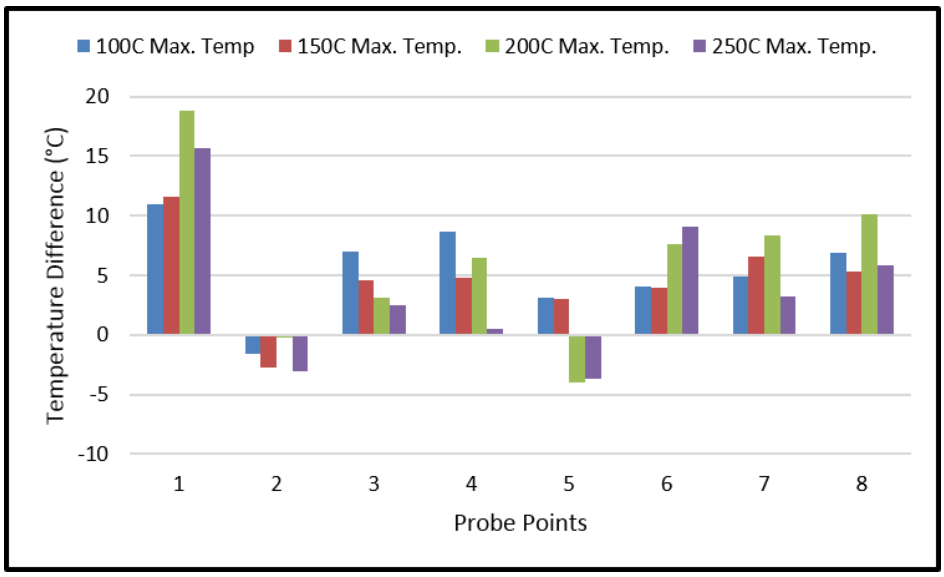

Figure 5.7: Zone 2 Absolute Temperature Offset Comparison

large offset of this one probe point temperature. The grid may need further refinement in this region in order to capture the proper temperatures as seen in experimentation.

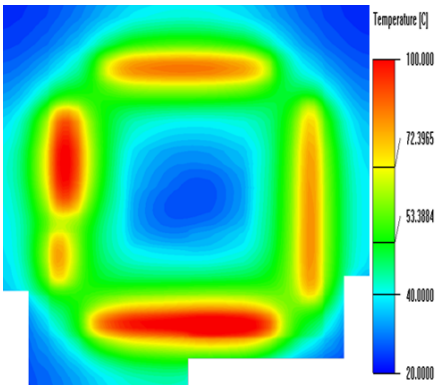

(a) Zone 3 100°C- Computational

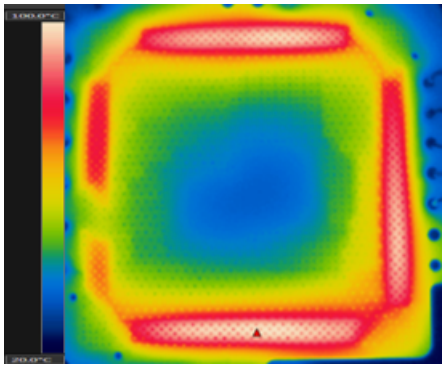

(b) Zone 3 100°C-Experimental

Figure 5.8: Zone 3 Single Heater Computational vs. Experimental Contour Plots (100°C)

Zone 3 singular zone computational and experimental contour plot results were similar to results from Zones 1 and 2. Zone 3, however, exhibited the largest difference between

computational and experimental probe points. See Figure 5.10 for the bar graph displaying results from the Zone 3 singular zone study. Probe point 2 showed the largest resulting difference during the 250°C maximum temperature trial with a value of 42°C. In contrast the remaining computational probe point temperatures are predicted within 30°Cat all remaining maximum temperature points. Finally, the Zone 4 computational and experimental

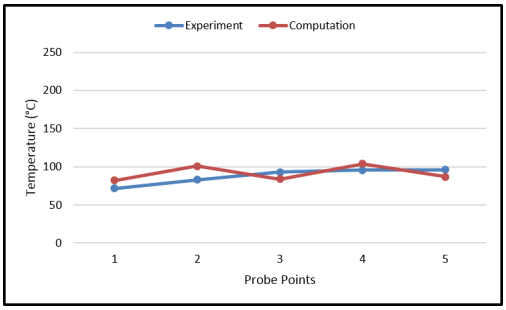

(a) 100°C Max. Temp. Probe Point Comparison

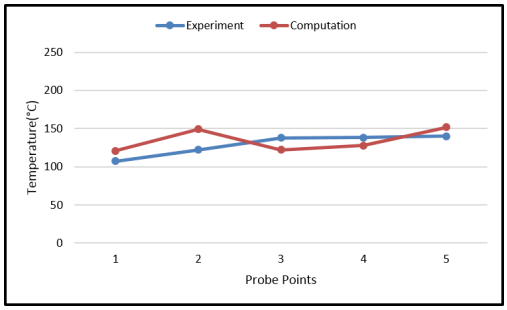

(b) 150°C Max. Temp. Probe Point Comparison

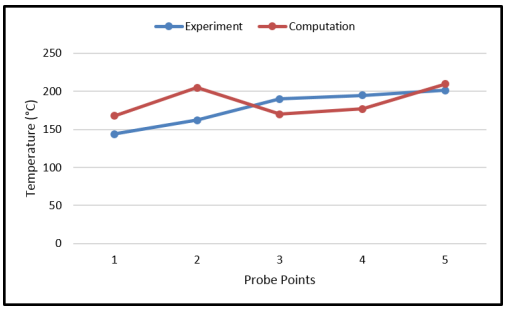

(c) 200°C Max. Temp. Probe Point Comparison

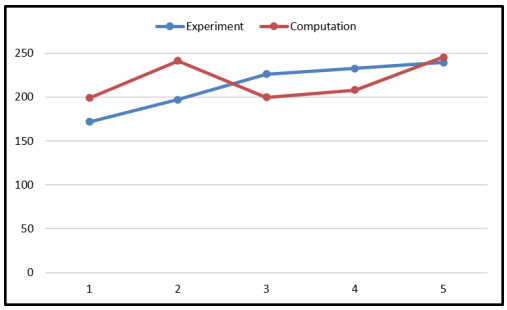

(d) 250 °CMax. Temp. Probe Point Comparison

Figure 5.9: Zone 3 Probe Point Comparison

contour plot results at the 100°C maximum temperature point, are presented in the contour plot comparison of Figure 5.11 the probe point comparison of Figure 5.12 and in the absolute temperature offset graph of Figure 5.13. Computational results of Zone 4 are similar to the preceding three zone studies. All probe points are either over predicting or under predicting the absolute temperatures within a 20°C offset, with the exception of probe point 1, as can be seen by referring to Figures 5.12 and 5.13. Probe point 1 is over predicting the absolute

temperature by a difference of 29°C, however, this probe point like others discussed before, is in an area of high heat flux. Due to the high heat flux, the grid meshing in this area may be refined in order to more accurately capture the absolute temperature in that region.

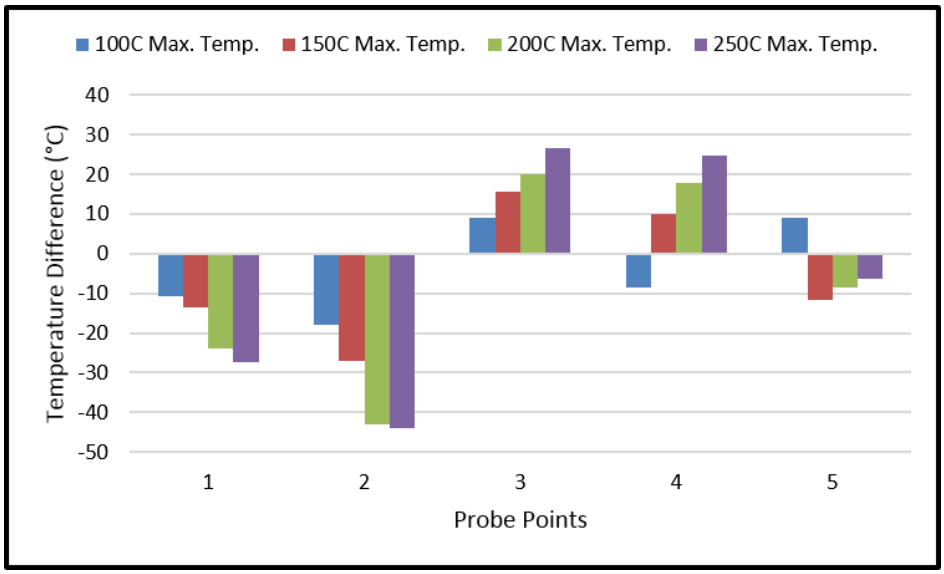

Figure 5.10: Zone 3 Absolute Temperature Offset Comparison

All computational singular zone studies resulted in similar outcomes. The computational contour plots agreed well with the corresponding experimental singular zone contour plots. The majority of probe point temperatures in the computational model either over or under predicting the absolute temperatures at the corresponding experimental probe points by no more than 20°C. However, there are a few outlying probe point temperatures that over or under predicted the absolute temperatures by 30-40°C. In these areas the mesh would need to be refined to better analyze the absolute temperature.

The majority of all probe points for each singular zone study at each maximum temperature trial, consistently under predicted the absolute temperature value at the corresponding probe points in the experimental trials. However, there were exceptions. Computational temperatures at probe points 2, 3, and 4 of Zone 2 behaved erratically by beginning with small differences as compared to experimental temperatures and increasing drastically after

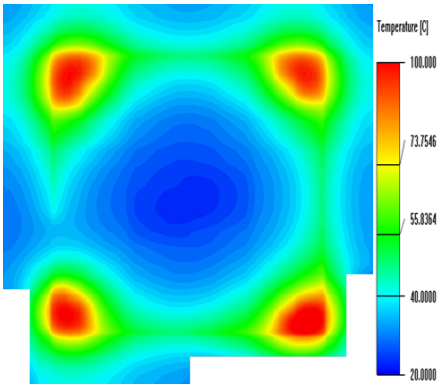

(a) Zone 4 100°C- Computational

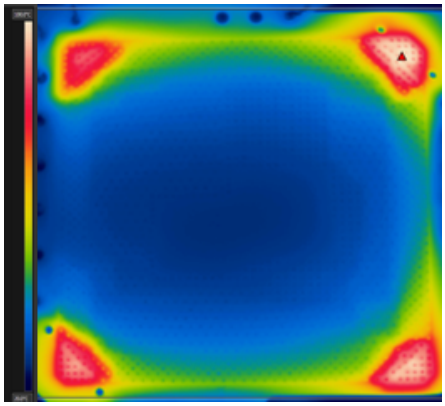

(b) Zone 4 100°C-Experimental

Figure 5.11: Zone 4 Single Heater Computational vs. Experimental Contour Plots (100°C)

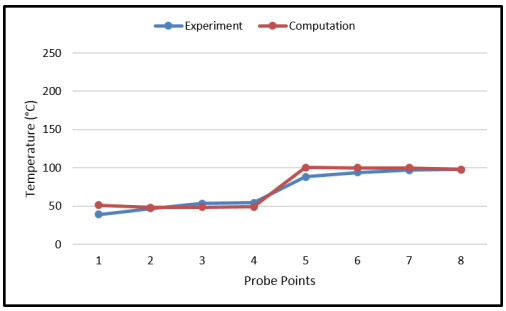

(a) 100°C Max. Temp. Probe Point Comparison

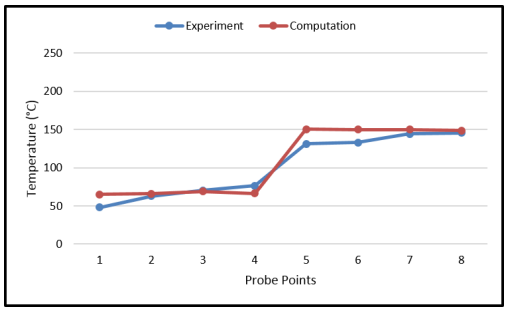

(b) 150°C Max. Temp. Probe Point Comparison

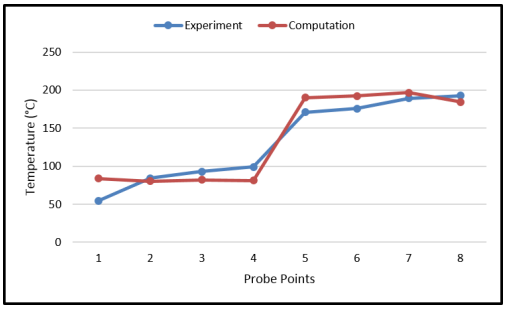

(c) 200°C Max. Temp. Probe Point Comparison

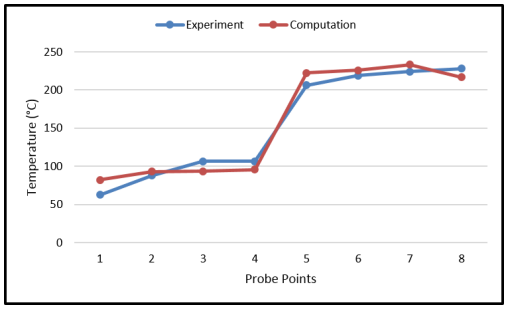

(d) 250 °CMax. Temp. Probe Point Comparison

Figure 5.12: Zone 4 Probe Point Comparison

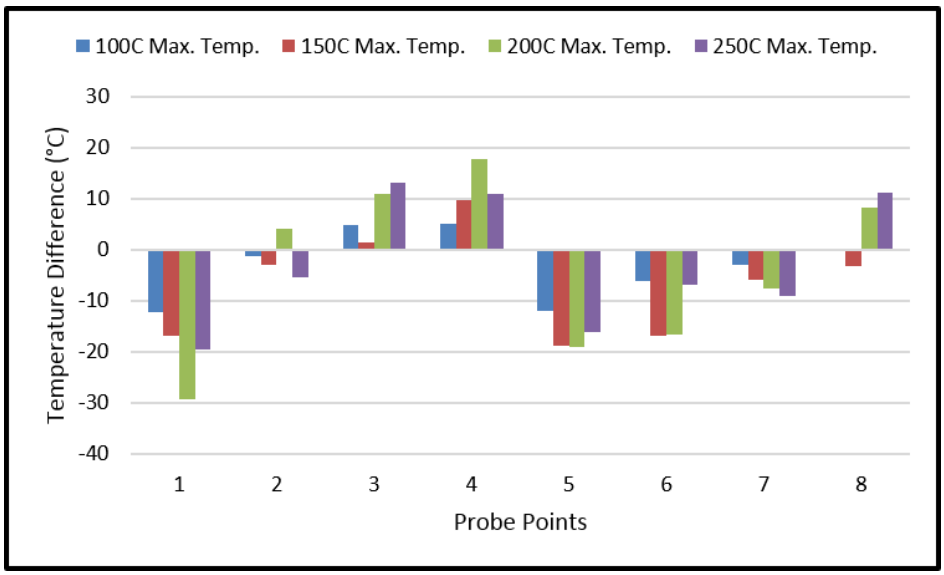

Figure 5.13: Zone 4 Absolute Temperature Offset Comparison

the 100°C maximum temperature trial. Probe point 10 of zone 3 over predicted the absolute temperature value at that particular location. And probe point 4 of Zone 4 also consistently over predicted the absolute temperature value during all four maximum temperature trials. It should be noted that each of these probe points that showcased behavior that differed from that observed in the other probe points, were situated in areas of high thermal gradients. Referring to Figure 5.1b see that probe points 2, 3, and 4 of Zone 2 are situated directly between an area of high temperature and relatively low temperature. The same can be observed for probe points 10 of Zone 3 in Figure 5.1c and probe point 4 of Zone 4 in Figure 5.1d. It appears that when absolute temperatures are computed at areas of extreme temperature gradients the computational model becomes erratic and cannot consistently estimate the absolute temperature.

Until this point, only the singular zone computational and experimental results have been discussed and compared. Multiple zone studies were also completed, where all four zones were powered on with the necessary amount of power to reach each of the four maximum temperature points specified (100°C, 150°C, 200°C, and 250°C). The resulting experimental

and computational contour plots are presenting in Figure 5.14 and Figure 5.15 respectively.

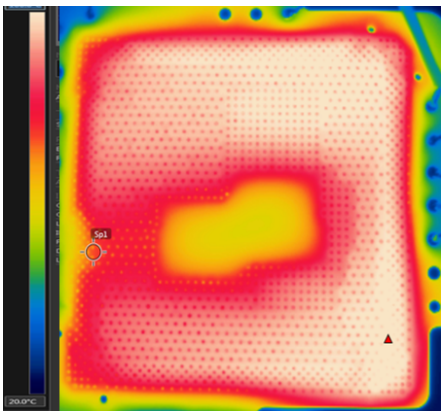

(a) 100°C Max. Temp. Multi-Zone

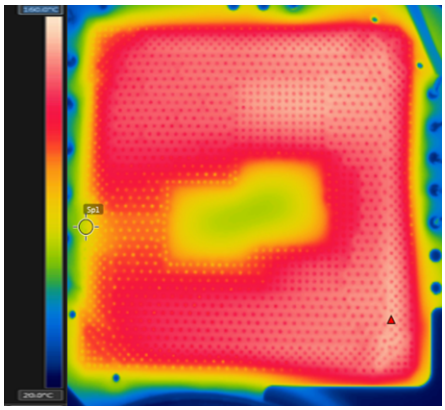

(b) 150°C Max. Temp. Multi-Zone

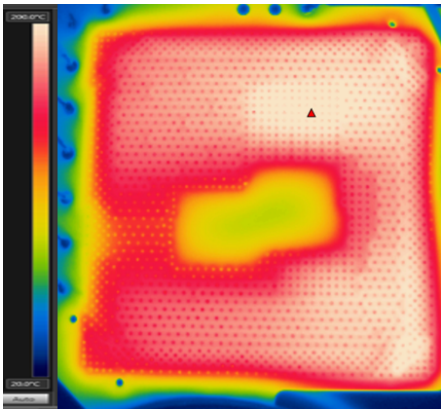

(c) 200°C Max. Temp. Multi-Zone

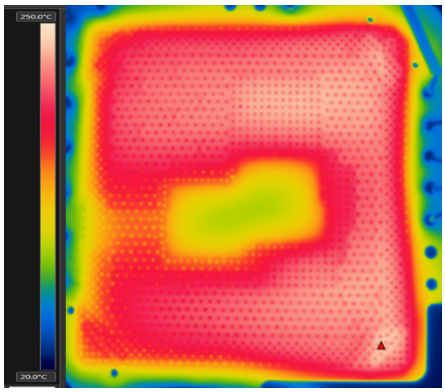

(d) 250 °CMax. Temp. Multi-Zone

Figure 5.14: Zone 4 Probe Point Comparison

The results in the multiple zone study are what would be expected based on the results from all singular zone studies. The contour plots of the computational studies match relatively well with the experimental contour plots, however the absolute temperatures start to diverge as the maximum temperature point is increased. See Figure 5.16 and Figure 5.17 to observe how the temperature difference increases for each probe point as the maximum temperature increases. Probe points 1 through 7 in Figure 5.16 are taken in the clockwise direction around the outside of the die shadow (cold region in center of ISRD). Probe point

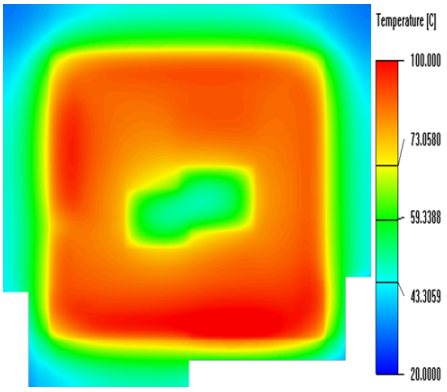

(a) 100°C Max. Temp. Multi-Zone

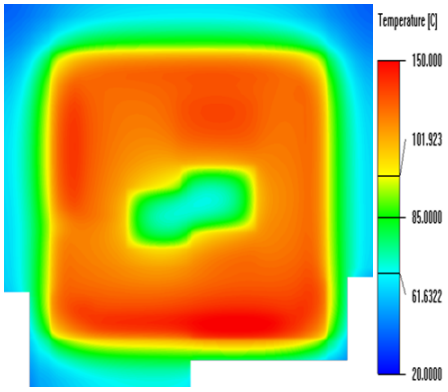

(b) 150°C Max. Temp. Multi-Zone

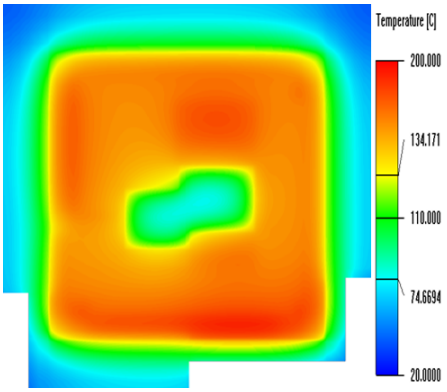

(c) 200°C Max. Temp. Multi-Zone

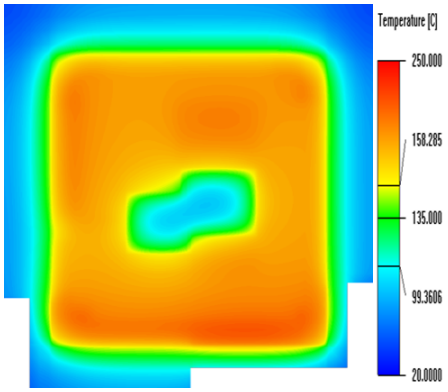

(d) 250 °C Max. Temp. Multi-Zone

Figure 5.15: Multi-Zone Computational Contour Plot Results With Altered Coefficient Value

8 is taken in the middle of the die shadow. Probe points 1, 7 and 8 seem to diverge the fastest when the 250°C maximum temperature point is reached. However, all other probe points seem to agree relatively well within 20°Cas was seen in the singular zone studies.

The heat transfer coefficient boundary condition for the multiple zone study was applied a crossed the entire surface of the ISRD computational model, instead of in discrete locations like the singular zone studies. Since the surface of the ISRD would theoretically be an isothermal surface, applying the heat transfer coefficient as a continuous boundary condition across all surfaces was most logical. The heat transfer coefficients applied to the surface

of each computational maximum temperature trial matched the heat transfer coefficients calculated for the single zone trials and can be referred to in Table 2.11. The resulting computational contour plots when using all theoretically calculated material properties and boundary conditions are presented in Figure 5.15.

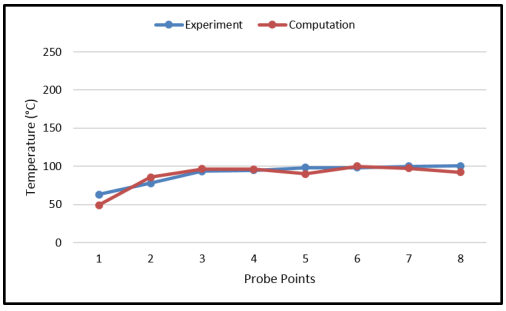

(a) 100°C Max. Temp. Probe Point Comparison

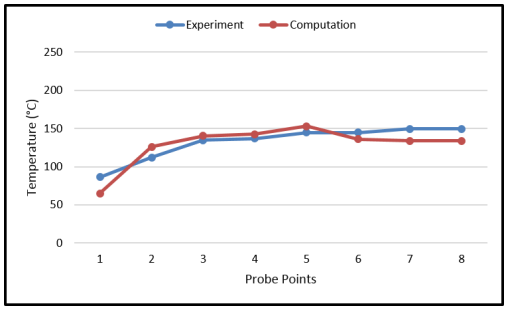

(b) 150°C Max. Temp. Probe Point Comparison

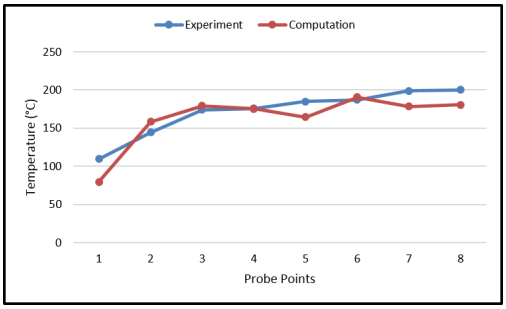

(c) 200°C Max. Temp. Probe Point Comparison

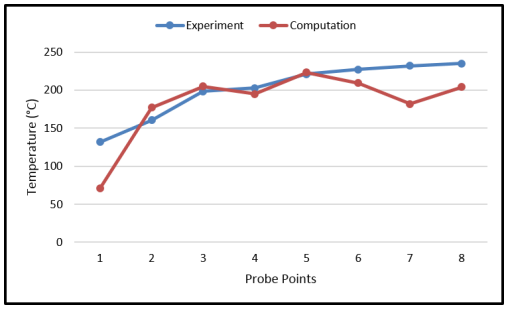

(d) 250 °CMax. Temp. Probe Point Comparison

Figure 5.16: Multiple Zone Probe Point Comparison

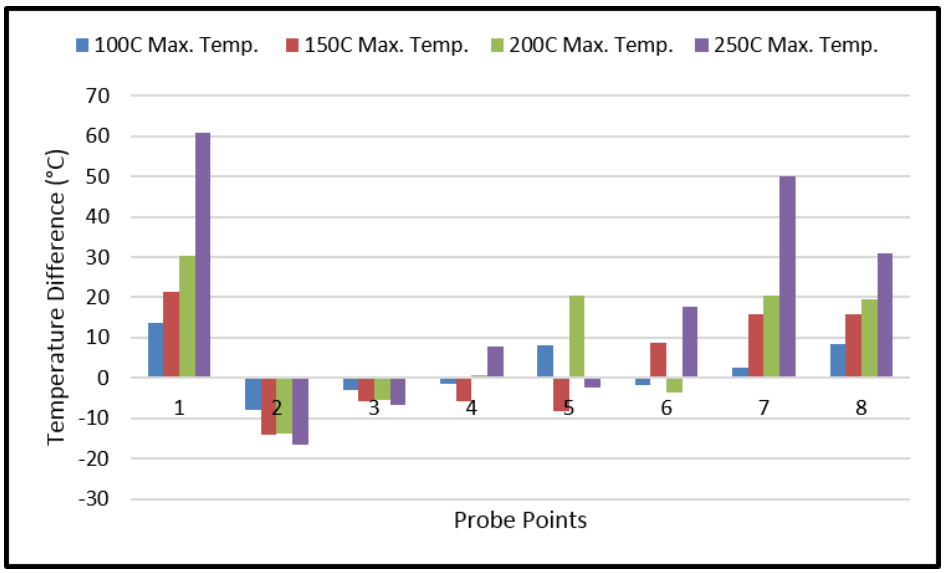

Figure 5.17: Multiple Zone Temperature Offset Comparison

CHAPTER 6

Summary and Conclusions

6.1 Summary

The goal of this project was to produce a bulk computational heat transfer model that could be used to predict gross thermal gradients within singular zones and across the top surface of an experimental ISRD as a result of a proposed heater trace design scheme. The development process for creating a geometrically simplified bulk computational model used to simulate internal heat transfer of the real ISRD was described in detail. The parameters that were theoretically calculated to create the computational model were: zone specific material properties based on varying via pitch values, external heat transfer boundary conditions at changing temperatures, heater zone shape, power allocation based on heater zone size, and entire ISRD shape. Experimental and computational trials were completed for correlation purposes in order to determine the abilities of the computational heat transfer model as a predictive tool for future heater design proposals.

To estimate the bulk material properties for application in the computational model, theoretical heat transfer conductivity equations were employed on four unit cells, representative of the four zones of the ISRD. Completing the conductivity equations resulted in unique orthotropic materials that simulate the varying conductivity as a result of the differing via pitch throughout the ISRD body. The orthotropic material properties were applied to respective zones within the computational model to simulate the thermal gradients observed across the ISRD surface as a result of varying FR-4 to via ratios.

To accurately model the geometry of the real ISRD, the internal heater zones were estimated as rectangular blocks within the Ansys IcePak computational model by dividing the real ISRD heater shapes into discrete rectangular prisms for a simplified computational analysis. The rectangular prisms were specified as conducting solids so IcePak would ignore the contact resistance between internally mated surfaces and treat the blocks as one continuous structure. The geometry of the model remained rectangular and allowed for a hex-dominant meshing scheme consisting of approximately 31,000 nodes to compute the results of several trial iterations. Low mesh count resulted in quick run times and exceptionally low computational expense.

The percentage of power allocation per heater zone was calculated by considering each heater zone size within the real ISRD. Appropriate power was allocated to each zone based on it's total surface area habitation within the entire ISRD. Power data from the corresponding singular and multiple zone experimental trials was utilized as an input to the computational model. Experimental trials were completed for singular and multiple zone studies to provide power and thermal data for input and comparison against the computational model, respectively.

The resulting contour plots and absolute temperatures from the computational study were compared to the experimental thermal data in order to determine if the calculated theoretical bulk parameters could produce a model with the ability to accurately predict the thermal capability of proposed ISRD heater design schemes. The contour plots of both the computational and experimental trials were compared independently and side by side. The ability of the computational model to predict absolute temperature values were studied by considering the offset of absolute temperatures at specified probe points with regards to corresponding probe points on the experimental trial contour plots.

6.2 Conclusions

The computational heat transfer model was found to be capable of predicting gross thermal gradients within single ISRD zones. The singular zone studies consistently produced contour plots that agreed well with the thermal contour plots of the experimental single zone studies. The hot and cold spots which were apparent in the experimental trials were captured in the computational results. Four maximum temperature points were tested for each of the computational and experimental single zone trials. The computational model consistently predicted the shape of the thermal contour plots as compared to the experimental thermal contour plots and did not diverge when tested at the low maximum temperature point (100°C) through the high maximum temperature point (250°C).

The computational model was also able to predict the absolute temperature points at certain probe point locations within 20°C of the absolute temperature of the corresponding probe points in experimental thermal images. Further grid refinement studies should be investigated in order to diminish the absolute temperature offset. However, without further grid refinement the single zone studies proved that the computational model can closely predict the majority of absolute temperature points to be within 20°C of the experimental temperatures.

The multiple zone studies were conducted at each of the four maximum temperature points that were specified for the single zone studies (100°C, 150°C, 200°C, and 250°C). The contour plots in the multiple zone study identified the same hot and cold spots as the experimental contour plots, however, the results were not as obvious as was observed in the single zone studies. As the maximum temperatures were increased, the contour plots continued to predict the correct hot spots versus cold spots.

The bulk ISRD model is suitable for use as a predictive simulation tool to analyze the gross thermal gradients that could potentially occur across the surface of an ISRD as a result of heater zone shape, ISRD shape, and via pitch. The ISRD model has the ability to predict

thermal gradients within single zones as well as multiple zones.

6.3 Future Work

The bulk ISRD model could be used to influence the direction of future ISRD heater trace designs. It has the potential to be used as a tool to provide quick feedback on the feasibility of the thermal capability of proposed heater designs, and could provide recommendations for creating better thermal uniformity across the ISRD surface. The bulk ISRD model has the ability to reduce design and prototype time and expense associated with developing ISRD's. Increased confidence and efficiency is the result of the predictive analysis capability of the bulk ISRD model.

The same development method described here can also be applied to the bulk simulation of a motherboard. Since the purpose of the ISRD is to simulate the thermal solution failure of a high powered component, in a laboratory test, the ISRD will be in contact with a motherboard. It is imperative to design an ISRD that takes the thermal impact of a motherboard into account. The motherboard is much larger and far more complex than the ISRD described in this paper, and therefore usage of a bulk computational model similar to the one developed for the ISRD would be of great value.

Appendix A

Figures for the comparison study between computational results and experimental data at maximum temperature points 150°C through 250°C can be found in this Appendix. The computational and experimental images are shown side by side for easy comparison of contour plots and absolute temperature values.

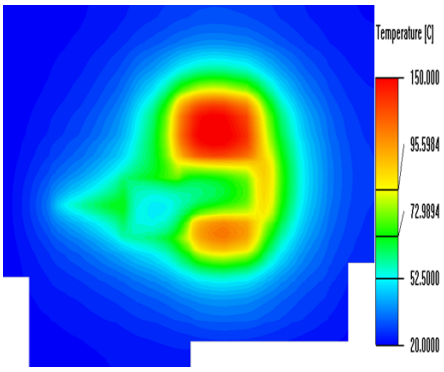

(a) Zone 1 150°C- Computational

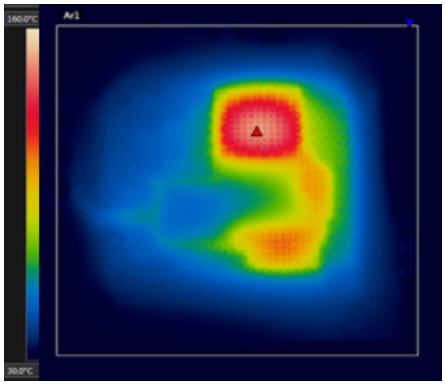

(b) Zone 1 150°C-Experimental

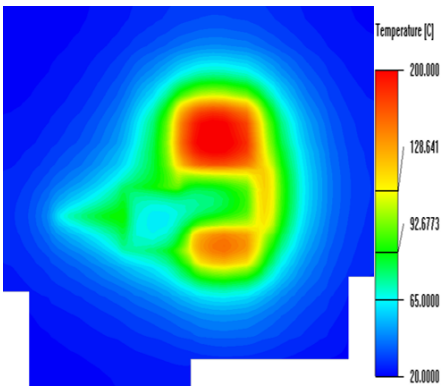

(c) Zone 1 200°C-Computational

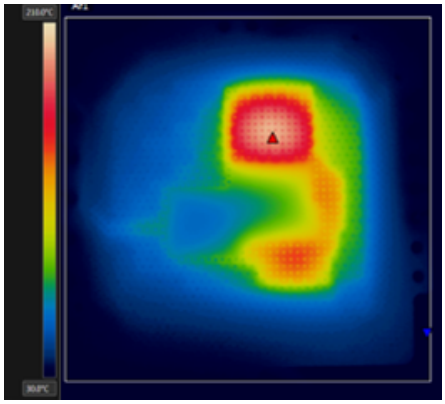

(d) Zone 1 200°C-Experimental

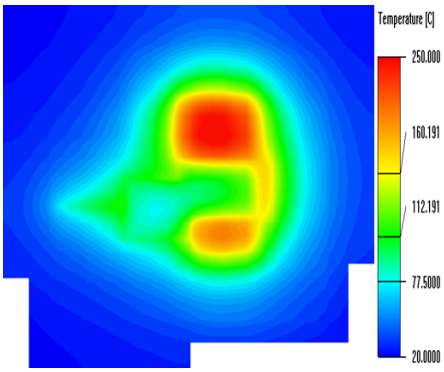

(e) Zone 1 250°C-Computational

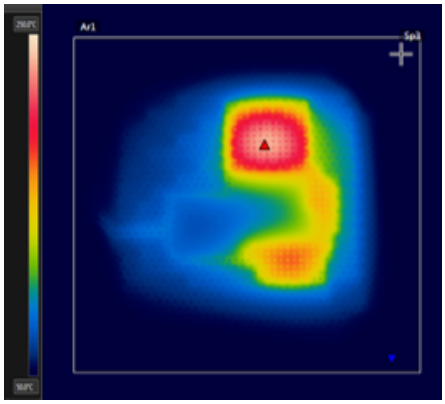

(f) Zone 1 250°C-Computational

Figure 1: Zone 1 Single Trace Computational and Experimental Contour Plot Comparison (150°C -250°C)

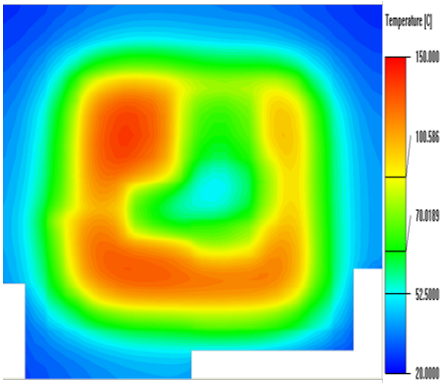

(a) Zone 2 150°C- Computational

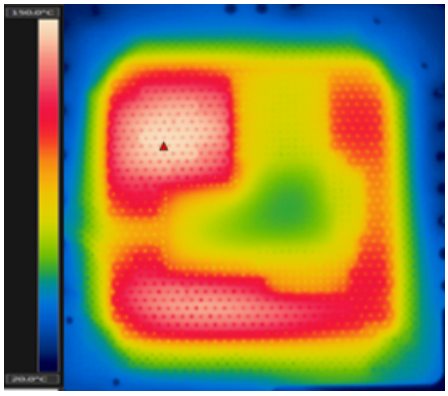

(b) Zone 2 150°C-Experimental

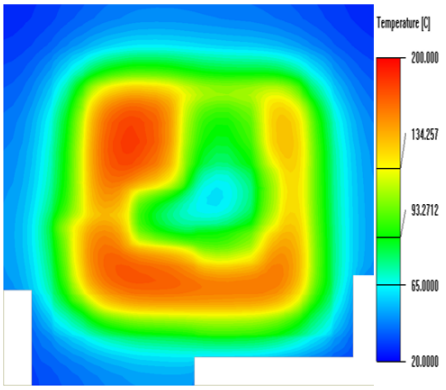

(c) Zone 2 200°C-Computational

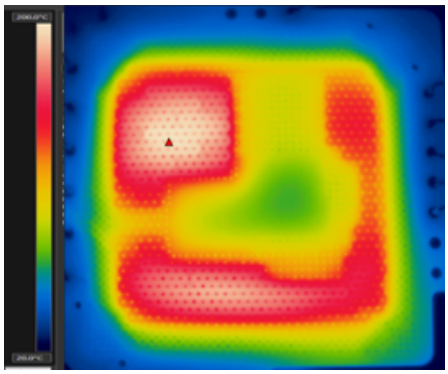

(d) Zone 2 200°C-Experimental

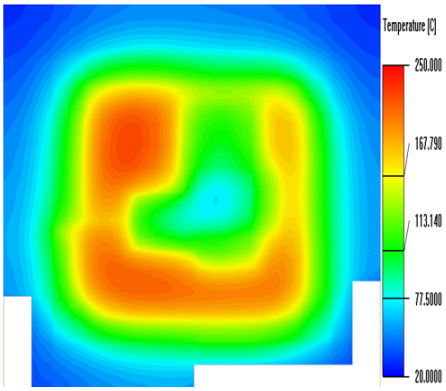

(e) Zone 2 250°C-Computational

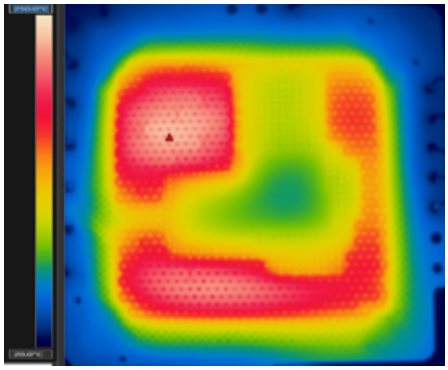

(f) Zone 2 250°C-Computational

Figure 2: Zone 2 Single Trace Computational and Experimental Contour Plot Comparison (150°C -250°C)

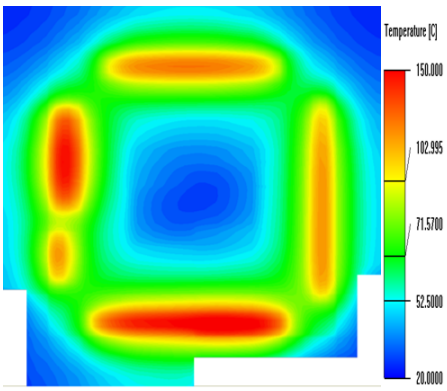

(a) Zone 3 150°C- Computational

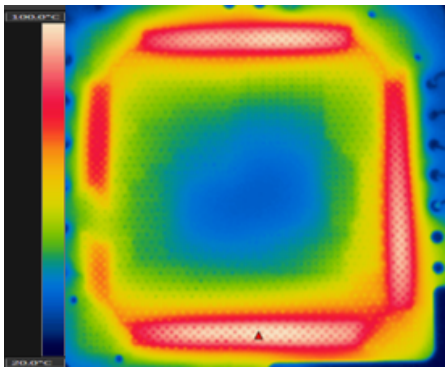

(b) Zone 3 150°C-Experimental

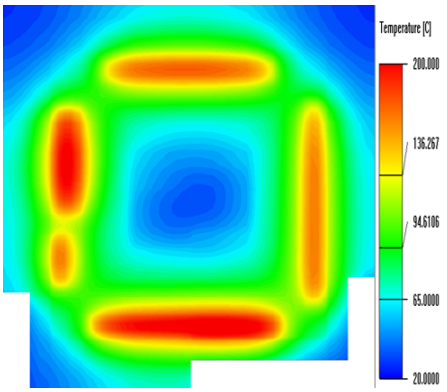

(c) Zone 3 200°C-Computational

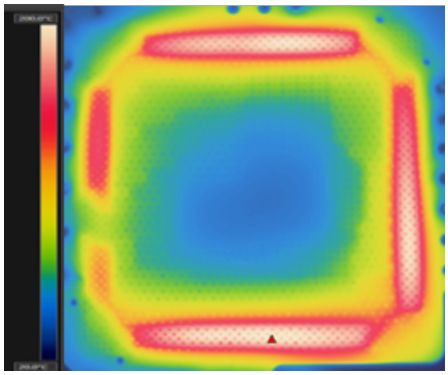

(d) Zone 3 200°C-Experimental

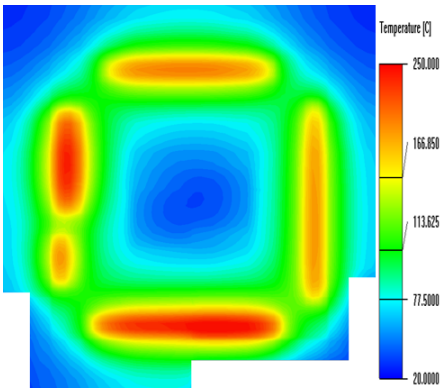

(e) Zone 3 250°C-Computational

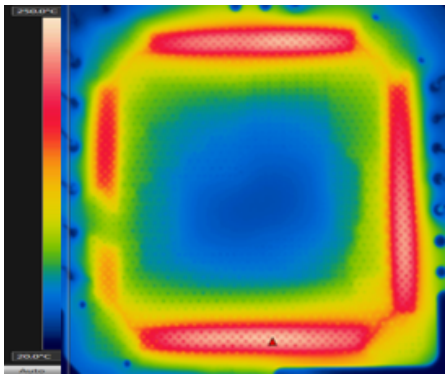

(f) Zone 3 250°C-Computational

Figure 3: Zone 3 Single Trace Computational and Experimental Contour Plot Comparison(150°C -250°C)

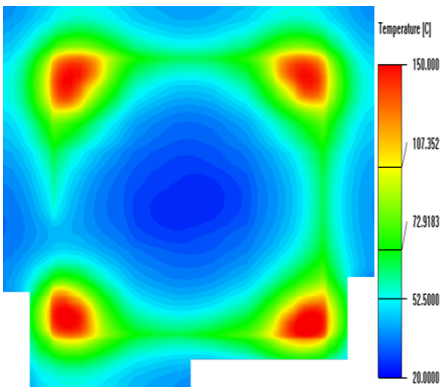

(a) Zone 4 150°C- Computational

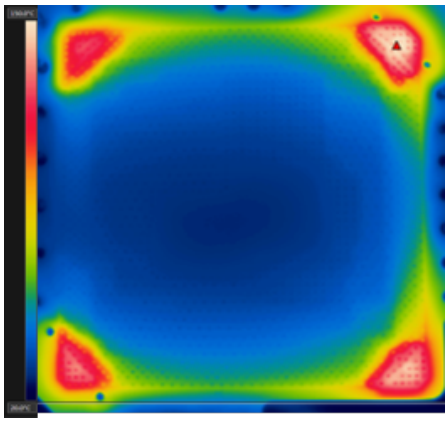

(b) Zone 4 150°C-Experimental

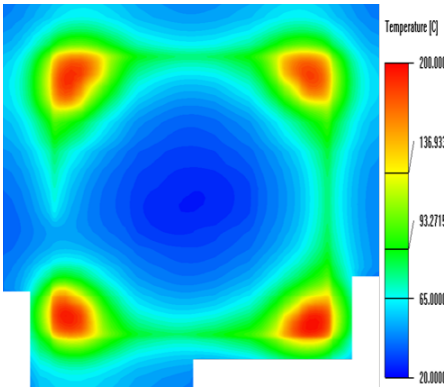

(c) Zone 4 200°C-Computational

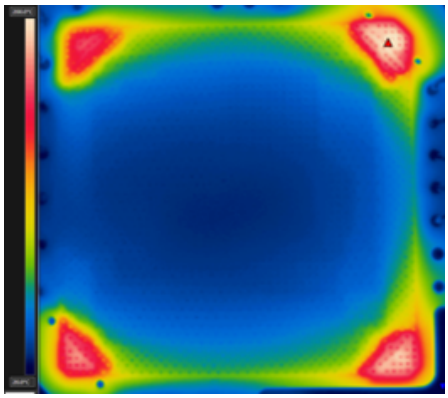

(d) Zone 1 200°C-Experimental

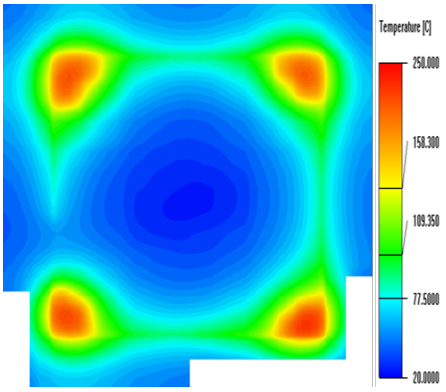

(e) Zone 4 250°C-Computational

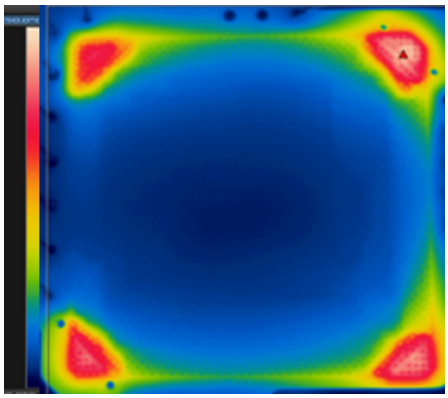

(f) Zone 4 250°C-Computational

Figure 4: Zone 4 Single Trace Computational and Experimental Contour Plot Comparison(150°C -250°C)

REFERENCES

[1] Cox, Norman R., *Reflow Technology Handbook*. Research, Inc., 1992. Web.

[2] Trucco, Horacio Andres.

[3] Ma, He, et al., "The development of effective model for thermal conduction analysis for 2.5D packaging using TSV interposer." *Elsevier: Microelectronics Reliability*. 2013. Web.

[4] Xing, X. Q., *Thermal Modeling and Characterization of Packaging with Through-Silicon-Vias (TSV) Interposer*. IEEE 13^{th} Electronics Packaging Technology Conference. n.p. 2011. Web.

[5] Chien, Heng-Chieh, et al., *Estimation for equivalent Thermal conductivity of Silicon-Through Vias TSVs Used for 3D IC Integration*. IEEE International Microsystems, Packaging, Assembly and Circuits Technology Conference. n.p. n.d. Web.

[6] Hoe, Yen Yi Germaine, et al., *Effect of TSV Interposer on the Thermal Performance of FCBGA Package*. IEEE 11^{th} Electronics Packaging Technology Conference. n.p. 2009. Web.

[7] Culham, Richard J., et al. *Factors Affecting the Calculation of Effective Conductivity in Printed Circuit Boards*. IEEE InterSociety Conference on Thermal Phenomena. n.p. 1998. Web.

[8] Bergman, Theodore L., et al. *Fundamentals of Heat and Mass Transfer*. 7th ed. John Wiley and Sons Inc. 2011. Print.